Interlayer Excitonic Spectra of Vertically Stacked MoSe₂/WSe₂ Heterobilayers

Roland Gillen

The optical spectra of vertically stacked MoSe₂/WSe₂ heterostructures contain additional "interlayer" excitonic peaks that are absent in the individual monolayer materials and exhibit a significant spatial charge separation in out-of-plane direction. A many-body perturbation theory approach is used to simulate the excitonic spectra of MoSe₂/WSe₂ heterobilayers with three stacking orders, considering both momentum-direct and momentum-indirect excitons. The small oscillator strengths and the optical responses of the interlayer excitons are significantly stacking-dependent and give rise to high radiative lifetimes in the range of 5–200 ns at low temperature for the "bright" interlayer excitons. Solving the finite-momentum Bethe–Salpeter Equation (BSE), the lowest energy excitation is predicted to be an exciton over the fundamental indirect band gap, with a binding energy of 220 meV. However, in agreement with recent magneto-optics experiments and previous theoretical studies, the simulations of the effective excitonic g-factors suggest that the low energy momentum-indirect excitons are not experimentally observed. The existence of "interlayer" *C* excitons with significant exciton binding energies and optical oscillator strengths is further revealed, which are analogous to the prominent band nesting excitons in mono- and few-layer transition-metal dichalcogenides.

1. Introduction

The experimental realization of graphene in 2004[1,2] inspired an ongoing search for novel energetically stable quasi-2D materials and a detailed experimental and theoretical study of the influence of their reduced dimensionality. Recent theoretical reports based on high-throughput screening and machine-learning methods suggest that several thousand exfoliable, and largely

Dr. R. Gillen
Department of Physics
Friedrich-Alexander University Erlangen-Nürnberg
Staudtstr. 7, 91058 Erlangen, Germany
E-mail: roland.gillen@fau.de

[iD] The ORCID identification number(s) for the author(s) of this article can be found under https://doi.org/10.1002/pssb.202000614.

unsynthesized, materials exist,[3,4] offering a rich pool of materials with diverse physical properties.

A particularly interesting and well-researched family of novel 2D materials are the transition-metal dichalcogenides (TMDCs) of molybdenum and tungsten with the structural formula MX_2 (with $M =$ Mo and W and $X =$ S, Se, and Te). These materials have been well known in their bulk phases, where they are indirect semiconductors with bandgaps in the range of 0.8–1.3 eV and assume a layered structure with hexagonal symmetry. Analogous to graphite, the atoms within the layers are bonded covalently, whereas the layers are bound together mainly through noncovalent interactions. Interestingly, it had been realized early that this interlayer interaction, albeit weak compared with the covalent intralayer bonds, has a significant effect on the electronic and optical properties of molybdenum and tungsten TMDCs: the fundamental bandgap is indirect in bulk and few-layer samples and increases with decreasing thickness due to quantum confinement effects and the attenuation of interlayer-coupling-induced splittings of the valence and conduction band edges. In the absence of interlayer coupling effects in the monolayer limit, the bandgap is direct, causing a strong enhancement of photoluminescence (PL) quantum yield for decreasing material thickness.[5–10]
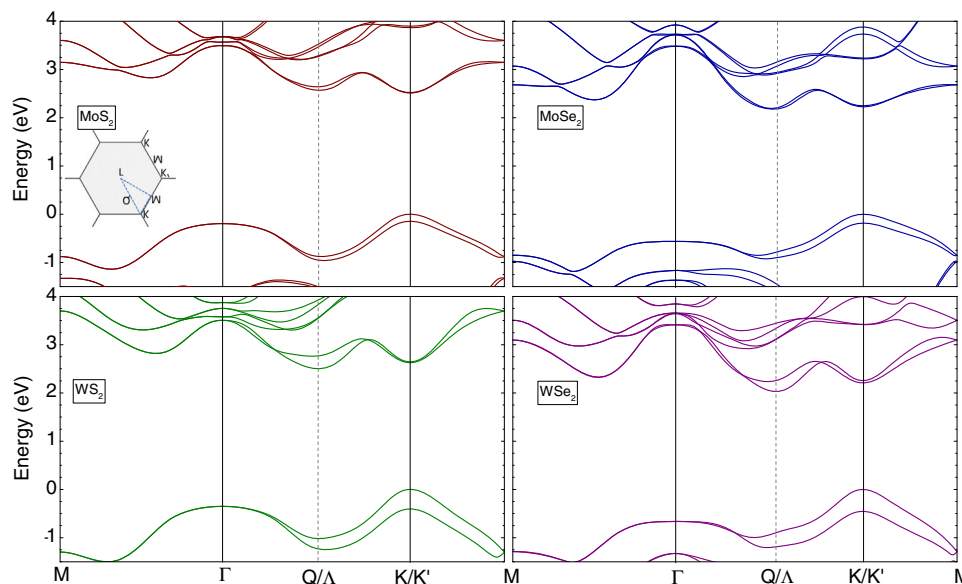
At the same time, the reduced dimensionality and highly non-local dielectric screening of Coulomb interaction give rise to rather large exciton binding energies on the order of 0.3–0.6 eV for monolayer molybdenum and tungsten TMDCs[11–19] despite the exciton wave functions to be rather expanded, with typical Bohr radii on the order of 2 nm.[19–21] Furthermore, the electronic band structures of molybdenum and tungsten disulfides, diselenides, and ditellurites show several local conduction and valence band extrema of similar energies; see **Figure 1**. This gives rise to a rich excitonic spectrum in mono- and few-layer TMDCs, dominated by "*A*" excitons originating from the direct bandgaps and, in few-layer materials, "*I*" transitions associated with the indirect fundamental bandgap. Interestingly, strongly bound "*C*" excitons appear at higher energies, between 2.0 and 3.0 eV, depending on the material, arising from a band nesting between valence and conduction band edges and an associated high-joint density at special points in the Brillouin zone.[20–22]

ADVANCED
SCIENCE NEWS
www.advancedsciencenews.com

physica
pss status
solidi b
www.pss-b.com

Figure 1. Calculated electronic dispersion of four monolayer molybdenum and tungsten dichalcogenides from simulations on the G_0W_0 level of theory.[98] The conduction band valley about halfway along the Γ–K/K' lines is typically labeled Q or by the Greek index L.

The strong spin–orbit interaction (SOI) introduced by the heavy transition metal atoms further leads to a prominent splitting of the valence band maximum at the corners of the 2D hexagonal Brillouin zones, allowing to exploit the circular dichroism for valley selective optical excitations with circularly polarized light. These findings inspired the use of mono- and few-layer TMDCs for a range of novel applications of TMDCs in novel thin and flexible optoelectronic devices, such as photodiodes,[23,24] photodetectors,[25] or single-photon emitters,[26–29] and for a combination of spin- and valleytronics.[30,31]

A possible way to further tailor the electronic and optical properties of TMDCs is the combination of different TMDCs to form vertically stacked heterostructures. Here, the noncovalent interlayer interaction in principle allows for atomically sharp and essentially strain-free interfaces even for lattice-mismatched materials, particularly interesting compared with conventional heterostructures formed of 3D bulk materials, where interfacial defects can have a significant effect on the material properties. Recently, the combination of Mo and W-based TMDCs arose substantial interest: for MoS_2/WS_2,[32] MoS_2/WSe_2,[33–35] $MoSe_2/WSe_2$,[36–40] and $MoSe_2/WS_2$[41,42] heterostructures, experimental observations indicate the presence of additional PL signals from excitations with the long lifetimes of 1–100 ns,[36,43,44] which are absent in the PL spectra of the individual monolayer materials.

The detailed origin of these transitions is still not entirely clear and might vary with the material combination and experimentally studied samples. Theoretical studies predict that the aforementioned heterostructures form type-II heterostructures with the valence and conduction band edges of the composite materials being localized in different layers.[45] For this reason, a reasonable and popular explanation of the observed signals is the attribution to interlayer excitons with a distinct spatial separation of the bound electrons and holes, an interesting concept for application in photovoltaics based on such heterostructures.[46]

These arguments are based on the assumption that the interlayer coupling between the individual materials is small enough that the electronic properties of the individual materials are largely unaffected. However, it is known from the TMDC homomultilayer materials, such as bilayer MoS_2, that the (rather weak) hybridization between S and Se p_z states in the different layers causes an interlayer-induced band splitting and a layer-number-dependent direct-to-indirect bandgap transition. At the same time, these additional signals are somewhat reminiscent of the "I" transitions in TMDC homobilayers and might indicate phonon- or defect-assisted emission over an indirect bandgap.

Due to the rather complex nature of the TMDC band structures with several conduction band and valence band valleys with similar energies and additional spin–orbit and interlayer coupling effects, a clear identification of the origin of these peaks is nontrivial and strongly depends on a comparison of experimental data with theoretical predictions of the electronic band structure, exciton binding energies, and the orbital composition of relevant bands. For instance, Kunstmann et al. used a correlation of the PL spectra in MoS_2/WSe_2 heterostructures with various twist angles with the respective band gaps from density-functional theory (DFT) calculations to attribute the prominent "interlayer" PL peak at around 1.6 eV to a momentum-indirect exciton, with the bound electron and hole being located at the K point and the center of the hexagonal Brillouin zone, respectively.[34] In addition, recent PL measurements on MoS_2/WSe_2 heterostructures encapsulated in boron nitride with small twist angle suggest the presence of an additional excitonic signal at an energy of about 1 eV, well below the fundamental bandgap of the heterostructure, with a significant Stark shift indicating a strong vertical separation of the electron–hole pair by about 6 Å. Based on theoretical simulations, this infrared peak was attributed to a transition between the global valence band maximum at the K point of the WSe_2 layer and the global conduction band minimum at the K point of the MoS_2 layer.[35]

For nearly lattice-matched $MoSe_2$/WSe_2 heterostructures, low-temperature experiments revealed that the prominent interlayer peak consists of a doublet of two separate contributions with a small energy difference of 25 meV. Due to the aforementioned complexities of the electronic band structure, the exact origin or these peaks is still a matter of debate. Depending on the experimental evidence and insight from theoretical calculations, the PL signals were attributed to 1) a mix of momentum direct ($K \rightarrow K$) and momentum-indirect ($K \rightarrow Q$) interlayer excitons, evidenced by the different temperature behaviors of the PL peak life-times;[36,43] 2) to a pair of momentum-indirect $K \rightarrow Q$ excitons, with an energy separation due to the spin–orbit splitting of the conduction band valley at the Q point, evidenced by the observed opposite circular polarization;[47] 3) a singlet–triplet pair of neutral, momentum-direct, excitons at the K and K' points, evidenced by recent measurements of the interlayer exciton PL under application of external magnetic fields;[48–51] and 4) a pair of spatially indirect neutral exciton and spatially indirect negatively charged trion, evidenced by an observed constant relative intensity of the two PL signals at low temperature,[40] but somewhat contradicted by the circular polarization response reported by other authors. For structurally similar MoS_2/WS_2 heterobilayers, experimental reports suggest the existence of three interlayer exciton peaks, which were attributed to $K \rightarrow K$, $Q \rightarrow \Gamma$, and $K \rightarrow \Gamma$ transitions based on a combination of optical measurements and theoretical simulations using the excitonic Bethe–Salpeter Equation (BSE).[52]

An alternative explanation for the origin of the observed interlayer exciton peak structure is offered by the effects of the intrinsic (albeit small) lattice mismatch and small deviations in relative twist angles from the symmetric stacking orders in studied samples, giving rise to long-period moiré superlattices and corresponding moiré potentials, which might activate, otherwise, optically forbidden spin-flip transitions[48] and allow for a moiré trapping and localization of excitonic states in the minima of the moiré superlattice potential,[53] of significant potential interest for manipulation of excitons in van-der-Waals heterostructures. In addition, the differences in local stacking order have been shown to affect the interlayer exciton binding energies, oscillator strengths, and optical selection rules.[54] Based on magnetoluminescence experiments, a recent study suggested that the interlayer PL peaks in twisted $MoSe_2$/WSe_2 heterobi- and trilayer systems in R registry arise from moiré potential modulated momentum-direct and phonon-assisted momentum-indirect interlayer exciton emissions.[51]

On the theoretical side, accurate ab initio investigations of the excitonic spectra of van-der-Waals heterostructures are limited to rather small and symmetric systems due to the delicate interplay of quasiparticle band structure, effects from interlayer interaction and spin–orbit coupling and (computationally expensive) Coulomb interaction between electrons and holes. Despite these constraints, a number of studies using various methods have been reported recently, typically focusing on the properties of momentum-direct interlayer excitons[52,54–59] and trions.[58] On the other hand, to the best of our knowledge, there is no reliable theoretical data so far on the binding energies and wave functions of momentum-indirect excitons, which could significantly contribute to the detailed understanding of the experimental observations of interlayer exciton emissions. Another question

that has not yet been addressed concerns the structure of the absorption above the intralayer bandgaps, which is dominated by "C" excitons with high binding energy and significant interlayer delocalization in TMDC homo-single- and -few-layer systems.[21] These "C" excitons have been found recently to lead to interesting resonant enhancement effects in Raman spectroscopy experiments on TMDC multilayer systems.[60,61] This raises the questions of whether similar excitons exist in TMDC heterostructures as well and how are they affected by changes in the electronic structure.

This article is structured as follows: In the first part, the excitonic spectra of molybdenum- and tungsten-based monolayer TMDCs will be introduced as a basis for the following discussion. In the second part, using the example of $MoSe_2$/WSe_2 heterobilayers, we will then review an electronic structure and absorption spectra for different stacking orders as obtained from state-of-the-art many-body perturbation theory calculations, which yield an accurate prediction of electronic bandgaps and exciton binding energies and wave functions, thus allowing for a direct comparison with experiment. In the third part, we will discuss the binding energies and wave functions of momentum-indirect excitons that might contribute to the experimentally measured optical spectra. In particular, our calculations suggest that the observed interlayer exciton doublet is unlikely to consist of a combination of momentum-direct and momentum-indirect excitons, in agreement with recent experimental evidence, and point toward an identification of the interlayer exciton doublet with the $K \rightarrow Q$ transitions. In the fourth part, we will show that the similarities in the electronic structure between $MoSe_2$ and WSe_2 monolayers should lead to the occurrence of "interlayer" C excitons in the excitonic spectra of $MoSe_2$/WSe_2 heterobilayers, with a significant degree of spatial separation between the bound electrons and holes and rather high exciton binding energies of 400 meV. We refer to the previous studies[21,54] for the theoretical details, unless indicated otherwise in the text.

2. Results and Discussion

2.1. Excitonic Spectra of Monolayer TMDCs

In contrast to common bulk semiconductor materials, the non-local dielectric screening of the Coulomb interaction in 2D materials introduces a significant Coulomb interaction between optically excited electron–hole,[62] necessitating an explicit inclusion of electron–hole coupling effects in calculations not only for a proper description of oscillator strengths of optical excitations, but also for accurate exciton binding energies.

Figure 2 shows the imaginary parts of simulated dielectric functions of the widely researched monolayer molybdenum- and tungsten-based disulfides and diselenides,[21] in good qualitative and quantitative agreement with recent theoretical reports by other groups and consistent with experimentally measured absorption.[63,64] For all four considered materials, the Coulomb attraction is sufficiently strong to pull a number of prominent absorption peaks well below the single-particle absorption onset given by the direct electronic bandgaps. An analysis of the calculated excitonic wave functions, as shown
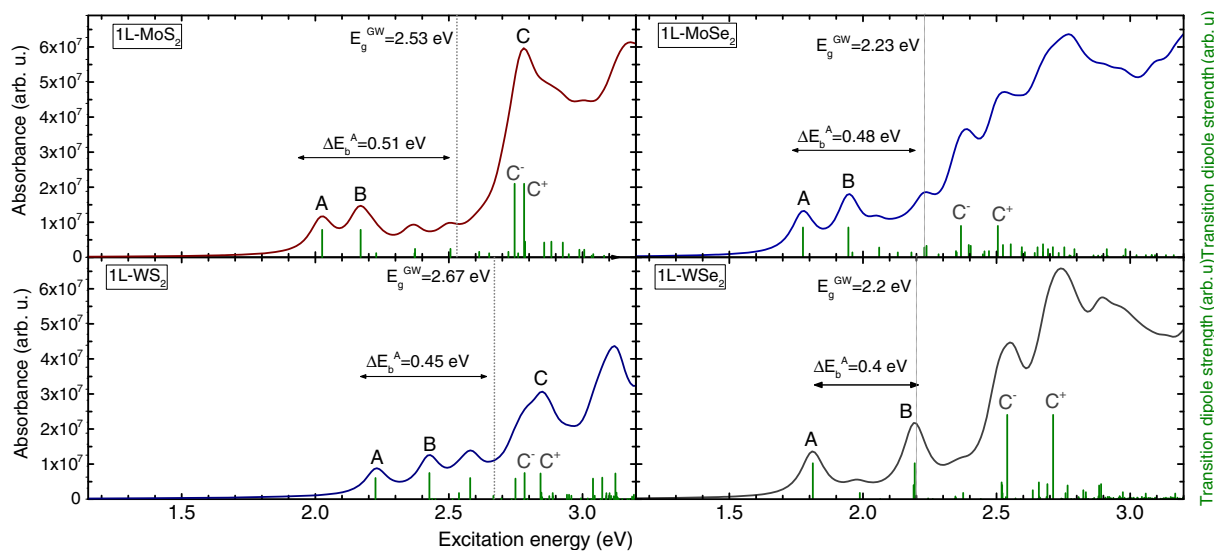
Figure 2. Calculated imaginary parts of the dielectric functions of four materials, including electron–hole coupling effects. MoS_2 and $MoSe_2$—Adapted with permission.[21] Copyright 2017, IEEE. The absorption spectra were shifted to match the electronic bandgap with the corresponding direct gaps in Figure 1. The absorption spectra of WS_2 and WSe_2 were calculated based on the electronic structure shown in Figure 1, following the method outlined in the previous study.[21] The absolute peak positions are slightly overestimated compared with experiment due to the neglect of temperature effects, which, for instance, can cause a redshift of the predicted A and B peak positions in MoS_2 by about 0.1 eV.[99]
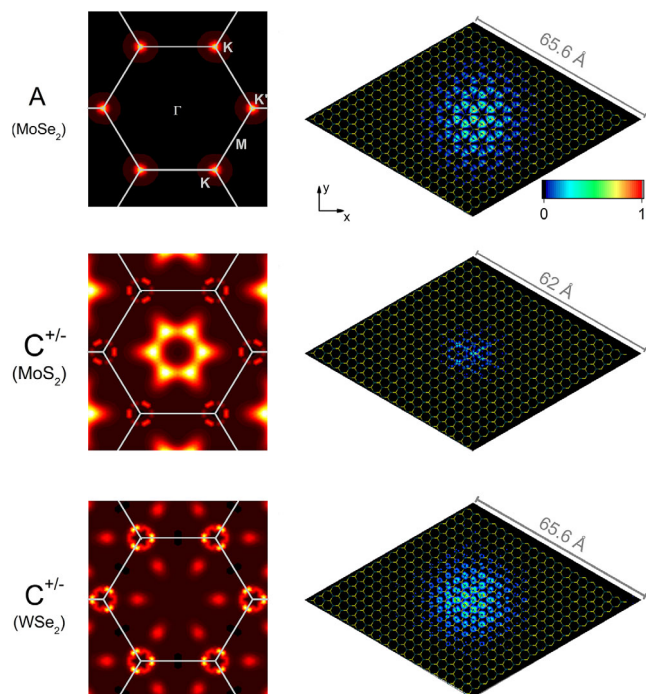
Figure 3. Calculated exciton wave functions of selected A and C excitons. The left-hand side of the subfigures shows the k-resolved contributions of transitions to the exciton wave functions. The right-hand side shows the top views of the spatial extent of the electron part of the exciton wave functions. For all excitons, the hole was fixed at a transition-metal atom in the center of the supercell of 20×20 unit cells that was used for the plot (arrows). Adapted with permission.[21] Copyright 2017, IEEE.

for $MoSe_2$ in **Figure 3**a, suggests that the lower-energy "A" peak originates from spin-conserving transitions over the direct bandgaps at the K and K' points in the hexagonal Brillouin zone. With this information, one can directly calculate the binding energy of the "A" electron–hole pairs as the difference between the exciton peak position (i.e., the optical bandgap) and the corresponding electronic bandgap. Here, a minor complication arises for tungsten-based materials, where the spin order of the spin–orbit split conduction band minimum at the K and K' points is reversed compared with molybdenum-based TMDCs; the lowest-energy direct transition between the valence band maximum is optically dark due to violation of spin conservation, whereas the transition to the second-lowest conduction band is optically bright.[65] With these considerations in mind, recent theoretical calculations yielded binding energies in the range of 0.4–0.5 eV for the four considered monolayer materials,[21,66–71] well within the range of 0.3–0.5 eV reported from experiments.[18,19]

The large excitonic binding energies are mirrored in the significant spatial localization of the excitonic wave functions compared with typical length scales of Mott excitons in 3D semiconductor materials; we find Bohr radii on the order of about 2 nm for the "A" excitons in all four materials (refer to right-hand side of Figure 3a). The "B" peak arises from an excitonic transition between the energetically lower sub-band of the spin–orbit split valence band maximum at the K/K' points to the spin-matched sub-band of the spin–orbit split conduction band minimum, thus appearing at slightly higher energies (mainly determined by the value of the spin–orbit splitting of the valence band), but with similar excitonic wave functions and exciton binding energies. The valence and conduction band extrema are completely spin-polarized at the K and K' points, with the

electron spin pointing in out-of-plane direction and the spin order at the three K' points of the hexagonal Brillouin zone reversed compared with the K points,[65] thus allowing for a valley-selective excitation of the A and B excitons using circularly polarized light.[72]

For monolayer MoS_2 and WS_2, the absorption spectra feature an additional prominent peak at an energy of about 2.75 eV, consistent with the broad "C" feature at this energy in experimentally measured absorption spectra.[14,63] Based on a decomposition of the calculated absorption spectra into the contributing transitions, the origin of this feature has been attributed to weakly spin–orbit split transitions between the valence and conduction bands at six points approximately halfway between the Γ point and the "Q" conduction band valley,[20–22] refer to the momentum-resolved exciton wave function in Figure 3b. To avoid confusion, we note that it is common in the literature to label this valley by the index L for the monolayer materials.

Using the value of the electronic bandgap close to these six points, we derived a significant exciton binding energy on the order of 700 meV for MoS_2, which is reflected in a small spatial extend of the exciton wave function (right-hand side of Figure 3b). The location of the C excitations in the Brillouin zone appears somewhat unusual on first glance, as, in contrast to the A and B excitons, they do not correspond to transitions between valence and conduction band extrema. Instead, the C exciton arises from a "band nesting" of transitions between the approximately parallel valence and conduction bands halfway along the Γ-Q line, see **Figure 4**a, thus leading to a high joint density of states and a correspondingly high optical oscillator strength and optical conductivity.[22]

As a consequence of this band nesting condition, it is to be expected that the location in the Brillouin zone, peak energy, and optical oscillator strength of the C exciton or corresponding excitations should significantly depend on details of the electronic dispersion. As Figure 1 shows, the dispersion around the valence band maximum of $MoSe_2$ and WSe_2 is flatter, and the conduction band dispersion is larger than in the disulfides, suggesting an increased repulsion between the transition metal d and chalcogen p states that make up the valence band ($d_{z^2}+p_z$) and the conduction band ($d_{xz,yz}+p_{x,y}$) edges at the Γ point.[65] This weakens the band nesting condition on the Γ-Q line (refer to Figure 4b for the example of monolayer WSe_2) and increases the difference between the transition energy at the band nesting

points and the direct bandgap of the system. At the same time, a set of six new band nesting points appear about halfway on the Q-K and Q-K' lines. The absorption spectra of $MoSe_2$ and WSe_2 feature two particularly bright transitions, which give rise to two prominent broader features above an energy of 2.5 eV (Figure 2). The calculated exciton wave functions (Figure 3c) suggest that these excitations have significant contributions from transitions at the "new" band nesting point and, hence, can be interpreted as C excitons as well, albeit of a different origin than the C excitons in the disulfides. A significant qualitative consequence arises from the fact that the valence band edge at the band nesting point in monolayer $MoSe_2$ and WSe_2 retains some of the spin–orbit splitting from the K and K' points, giving rise to two bright C excitations with a significant energetic splitting, in contrast to the very small splitting in the case of the disulfides. Similar results were found for monolayer $MoTe_2$ as well.[21]

Another effect on the C excitons of TMDC materials could arise from interlayer or substrate interaction. The significant contributions from chalcogen p states couple at the interface to adjacent materials, for instance, a neighboring layer in bilayer MoS_2, and lead to hybridization-induced band splittings. Despite this interlayer hybridization, we reported previously[21] that the resulting changes in the electronic dispersions are sufficiently small to retain the C excitons of the monolayer materials. In this context, the chalcogen p contributions at the band nesting points have interesting consequences in terms of the spatial extent of the A and C exciton wave functions. At the K and K' points, the valence band maximum and conduction band minimum are composed almost entirely of transition metal $d_{x^2-y^2} + d_{xy}$ and d_{z^2} orbitals, respectively, causing a negligible overlap and hybridization between the sub-bands of each material layer, particularly in light of the additional effect of spin–orbit coupling. As **Figure 5** shows for the example of MoS_2, this leads to a strong confinement of the electronic part of the exciton wave function to the layer where the hole is located. The A exciton in a molybdenum or tungsten TMDC homomultilayer should, hence, behave like the A exciton of the corresponding monolayer material. For the C excitons, the chalcogen p contributions to the conduction band result in a strong interlayer nature of the excitonic wave function, being significantly delocalized over the layers neighboring the layer where the hole is located. This interlayer nature might allow to resonantly couple a TMDC few-layer structure through optical excitation at the energy of C exciton, for instance,
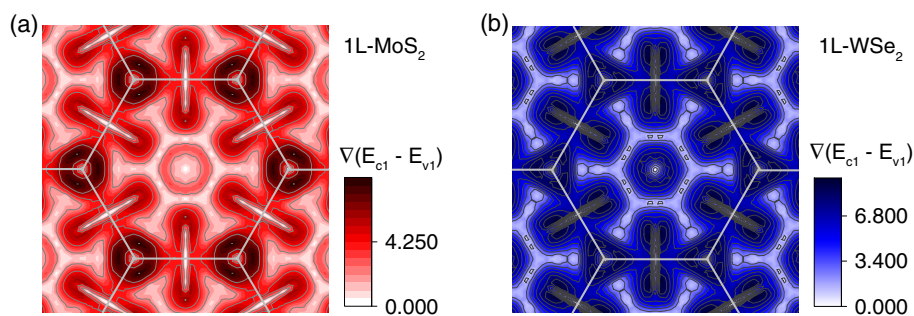
Figure 4. Difference between the energy gradients of the highest valence band (v_1) and the lowest-energy conduction band (c_1) plotted over the Brillouin zone for a) monolayer MoS_2 and b) monolayer WSe_2. Similar figures are obtained for WS_2 and $MoSe_2$ as well.
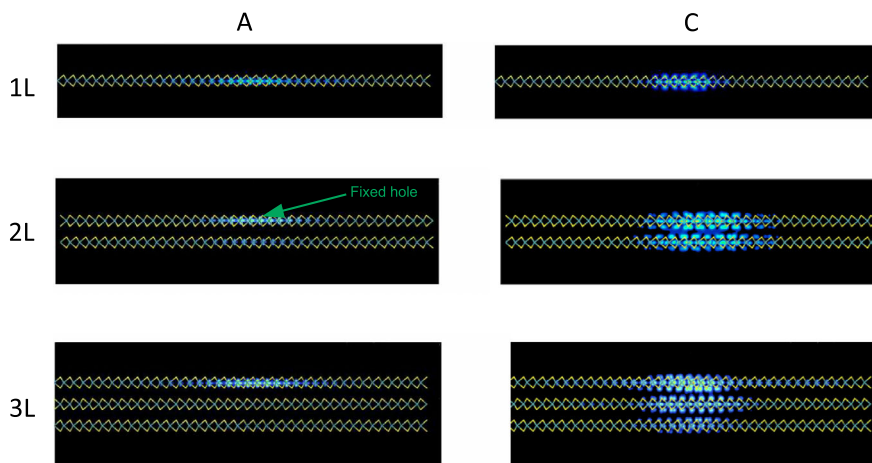
Figure 5. Side views of the electron parts of the A and C exciton wave functions of mono-, bi-, and trilayer MoS$_2$. In all cases, the hole was fixed at a molybdenum atom in the center of the 20 × 20 supercell used for the plot. Adapted with permission.[21] Copyright 2017, IEEE.

activating interlayer resonant Raman modes in few-layer TMDCs[60,73,74] that are not observed for excitation at the A exciton.

2.2. Electronic Band Structure of MoSe$_2$/WSe$_2$ Heterostructures

In the following, we will first summarize our previous results[54] on the electronic band structures and excitonic absorption spectra of lattice-commensurate MoSe$_2$/WSe$_2$ heterostructures with different stacking orders.

Figure 6 shows the electronic bands of vertically stacked MoSe$_2$/WSe$_2$ heterostructures obtained from GW calculations, which typically predict the electronic structures of materials with high accuracy, and were reported previously in the previous study.[54] To estimate the influence of interlayer coupling on the electronic band structures of these heterostructures, we tested three different stacking orders that preserve the hexagonal symmetry. In the AA stacking order, the metal and selenium atoms of the two monolayers are located on top of each other. AA′ stacking corresponds to the AA stacking order with the upper layer rotated by 60° relative to the lower layer and is the energetically most stable stacking order in homobilayer and bulk TMDCs. In the AB stacking order, on the other hand, the upper layer is shifted by $1/3(\vec{a}_1 + \vec{a}_2)$ compared with AA stacking. Both AA and AB stacking orders are of R-type due to their similarity to the stacking order in multilayer 3R-TMDCs, whereas AA′ stacking is of H-type due to its similarity to the layer arrangement in 2H-TMDCs.

For all three stacking orders, the bands at the K point of the hexagonal Brillouin zone show only a weak hybridization, so that the bands can be directly assigned to the individual layers. This behavior is not unexpected, as the valence and conduction bands at the K and K′ points arise largely from transition-metal d states and, hence, should only weakly "feel" the neighboring layer. Indeed, the bands form a type-II alignment, with the (global) valence band of the heterostructure contributed by the WSe$_2$ layer, whereas the conduction band minima at the K and K′ points are located in the MoSe$_2$ layer. The momentum-direct interlayer bandgaps between these bands are somewhat

stacking-dependent. As it is to be expected that AA and AB are the stacking orders with the weakest and strongest interlayer coupling for all possible twist angles between the layers, the bandgaps between K and K′ of the individual materials should generally fall within the range of 1.65–1.75 eV. Our calculations further indicate that the intralayer bandgaps at the K and K′ points of the individual materials are somewhat reduced by about 0.1 eV due to the dielectric screening provided by the respective other layers.

While the interlayer hybridization is very weak for the band around the K and K′ points, the situation is clearly different at other points in the Brillouin zone. The states at the local valence band maximum near the Γ point and the conduction band minimum near the Q point, about halfway along the Γ-K line, have significant contributions from Se p states and couple strongly between the layers. Similarly to the homobilayer materials, this interlayer coupling transforms the heterostructure into an indirect semiconductor. The contribution of orbitals from the WSe$_2$ layer to the conduction band minimum is stacking-order-dependent and increases from 20% for AA stacking to about 40% for AB stacking. Our results are in good agreement with other recent studies[57,69] and establish that vertically stacked MoSe$_2$/WSe$_2$ heterobilayers, contrary to previous predictions, only feature a pseudo-type-II band alignment and an indirect fundamental bandgap, which has possible implications for the nature and properties of the lowest-energy excitonic states of the material. Similar results have been found recently for MoS$_2$/WS$_2$ heterostructures as well.[57] In this case, the indirect fundamental bandgap has been predicted to be between the gamma and the K/K′ points, due to the smaller energy separation of the valence band maxima at the Γ and K points in the individual monolayer molybdenum and tungsten disulfides.

The electronic band structures of the materials suggest two possible origins for the additional "interlayer" excitonic peaks seen in PL experiments: 1) Transitions at the interlayer bandgaps at the K and K′ points of the Brillouin zone of the heterostructure. The optical strength of these transitions should then strongly depend on the twist angle between the materials, requiring an additional crystal momentum source for twist angles that
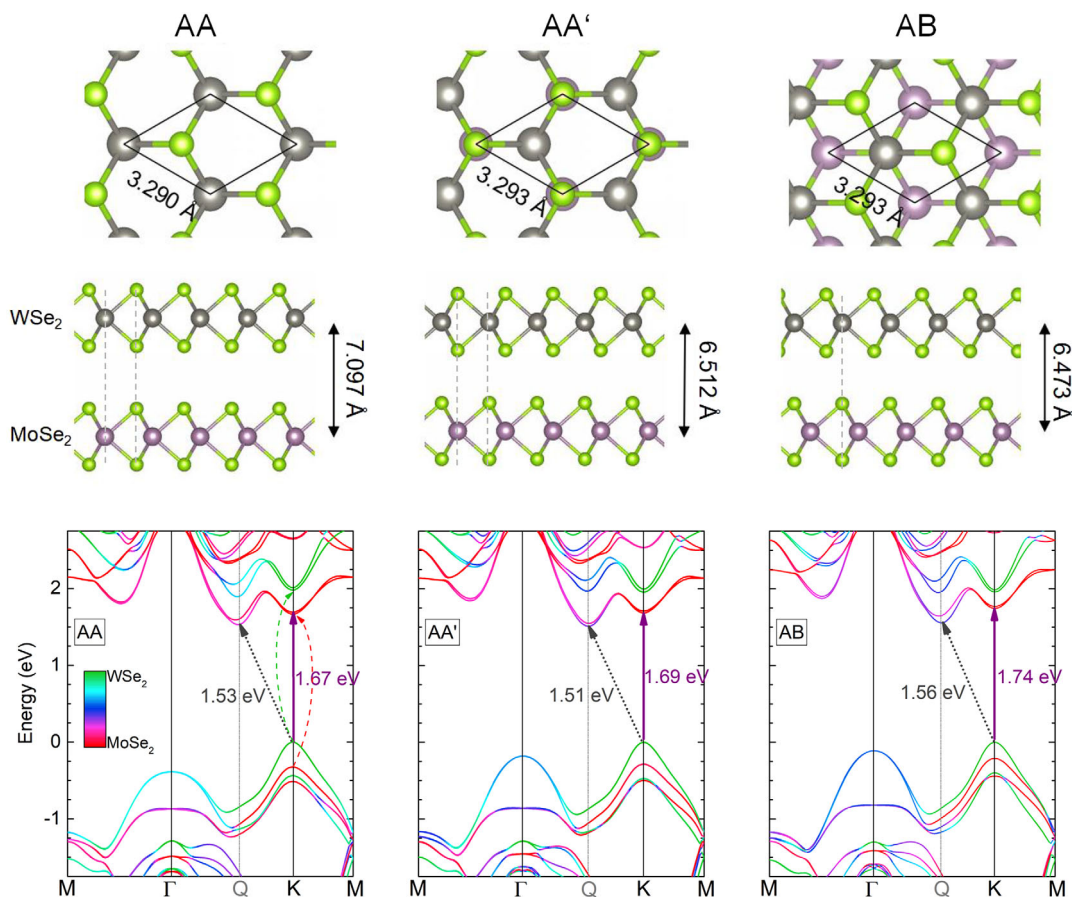
Figure 6. Atomic geometries and electronic band structures of $MoSe_2/WSe_2$ for three different hexagonal stacking orders. The color code for the band structures indicates the relative contributions of orbitals of the two sublayers to the bands and, hence, the degree of hybridization. Adapted with permission.[54] Copyright 2018, American Physical Society.

break hexagonal symmetry. 2) Transitions over the fundamental bandgap, which is indirect for all twist angles.

2.3. Momentum-Direct Interlayer Excitons in $MoSe_2/WSe_2$ Heterostructures

We recently reported the simulated absorption spectra of $MoSe_2/WSe_2$ heterostructures from solution of the excitonic Bethe–Salpeter equation, which includes effects from excitons with a vanishing center-of-mass momentum.[54] **Figure 7** shows the absorption spectrum for the AA′-stacked $MoSe_2/WSe_2$ heterostructure with the inclusion of spin–orbit coupling effects. The onset of absorbance is dominated by two transitions, Mo_A and W_A, which can readily be attributed to the A excitons of individual monolayer $MoSe_2$ and WSe_2: our analysis of the k-resolved contributions to the exciton wave function shows that Mo_A and W_A exclusively arise from intralayer transitions between the $MoSe_2$ (WSe_2) bands at the K and K′ points. Furthermore, the electron and hole parts of the excitonic wave functions show that the corresponding electron–hole pairs are completely confined to the $MoSe_2$ and WSe_2 layers, respectively (Figure 7). In principle, one could directly derive the exciton binding energies from a comparison of the peak positions in the calculated absorption

spectrum with the intralayer bandgaps from Figure 6. However, while the 21×21 k-point grid used in the calculation is sufficient to give a very accurate qualitative picture of the excitonic spectrum, it does not yield fully converged peak positions and exciton binding energies. A second calculation using a denser 33×33 k-point grid (without inclusion of spin–orbit coupling) yields the binding energies of about 310 and 290 meV for the Mo_A and W_A transitions, respectively, for the AA′ stacking order. This suggests that the additional dielectric screening induced by the neighboring layer reduced the binding energies of the intralayer A excitons by about 150 meV.

In addition to these intralayer excitons, the computed absorption spectra also reveal two series of peaks of small optical oscillator strength at lower energies; see inset of Figure 7. These peaks arise from interlayer transitions between the WSe_2-dominated global valence band maximum of the heterostructure to the spin–orbit split conduction band minimum at the K and K′ points; the X_n and Y_n peaks correspond to transitions to the lower energy and to the higher energy band, respectively. In the AA′ stacking order, the monolayer Brillouin zones of $MoSe_2$ and WSe_2 are rotated by 60° relative to each other; i.e., the K points of one material coincide with the K′ points of the other material. As a consequence, the Y_0 transition should be brighter than the lower energy X_0 transition due to spin
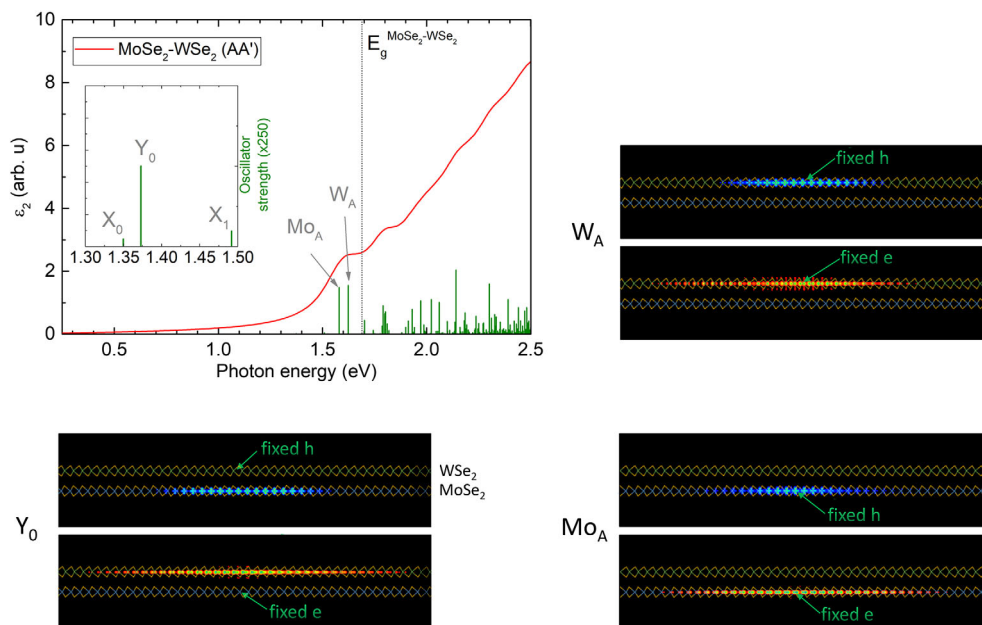
Figure 7. Simulated absorption spectrum of a $MoSe_2$/WSe_2 heterostructure with AA′ stacking order. Green lines indicate the individual transitions that give rise to the spectrum. Density plots show the electron (red density) and hole (blue density) contributions to the wave functions of three selected inter- and intra-layer excitons. The hole (electron) was fixed near a Mo or W site in the middle of a supercell of 21×21 unit cells for the plot of the electronic (hole) part. Adapted with permission.[54] Copyright 2018, American Physical Society.

conservation during the optical transition, whereas the X_0 transition should be dark in heterostructures with H-type stacking order. The excitonic wave function of the Y_0 transition is shown in Figure 7. In contrast to the Mo_A and W_A transitions, the exciton wave function shows a clear spatial separation of the electron and hole pairs between the layers. From calculations with a denser k-point grid, we derive a rather large exciton binding energy of about 250 meV, which is of similar magnitude as that of the intralayer excitons. Our calculations, thus, suggest that the X_n and Y_n peaks form two Rydberg series of interlayer excitons. Similar results were found for AA and AB stacking orders as well.[54] Our calculations, hence, support the initial assignment of these PL peaks to interlayer excitons from momentum-direct excitations over the interlayer bandgap at the K and K' points of the heterostructure. The low oscillator strength of these transitions is in agreement with recent photocurrent measurements in $MoSe_2$/WSe_2 p–n junctions, which suggested that the oscillator strength of the intralayer excitons is 200 times larger than that of the interlayer excitons.[75] On the other hand, Torun et al. recently pointed out that the high exciton lifetime due to the spatial separation of the electron–hole pair, in complete agreement with experimental investigation of the interlayer peak,[57] is much larger than the exciton thermalization time. The high interlayer peak intensity in PL spectra can, hence, be understood from a Boltzmann-type thermal occupation of excitonic states, which compensates for the low oscillator strength of the interlayer excitons due to the energy separation to the intralayer excitonic states.

Due to depolarization effects in out-of-plane direction, only light with parallel polarization to the materials surface should appreciably couple to excitons in 2D materials.[55] This is indeed the case for the AA and AA′ stacking orders, where either the X_0 or the Y_0 transitions are "bright" for parallel light polarization,

but dark for "perpendicular" light polarization that is parallel to the surface normal vector (see Supporting Information of the previous study[54] for a comparison). On the other hand, neither X_0 nor Y_0 shows any appreciable oscillator strength for AB stacking.[54] A detailed analysis revealed that this behavior can be traced back to variations in the optical selection rules for AB stacking compared with AA or AA′ stacking. The oscillator strength of the interlayer excitons largely arises from transitions between small contributions of $MoSe_2$ d states mixed into the valence band maximum at the K point into the $MoSe_2$-dominated conduction band. For AB stacking, these small contributions come from Mo d_z states, which causes the interlayer transitions to be optically active for perpendicular polarized light, albeit with a much smaller optical oscillator strength than for AA or AA stacking. These results suggest that the stacking order can have a marked effect on the coupling of interlayer excitons to polarized light. As we show in the following, the small oscillator strength also has strong implications for the radiative lifetime of interlayer excitons for AB-stacked $MoSe_2$/WSe_2 heterostructures.

Starting from Fermi's Golden rule, an expression for the computation of radiative lifetimes of excitonic states in 2D materials from the excitonic oscillator strengths can be derived.[55,76] Following this approach, the radiative recombination rate of the excitonic state s with a small center-of-mass momentum $\mathbf{Q}$ emitting light polarized parallel to the 2D material plane is given by

$$\gamma_s^{\parallel}(\mathbf{Q}) = \gamma_s \cdot \left(\sqrt{1 - \left(\frac{\hbar c^2 Q}{E_s(\mathbf{Q})}\right)^2} + \frac{1}{2} \frac{\left(\frac{\hbar c(Q_x - Q_y)}{E_s(\mathbf{Q})}\right)^2}{\sqrt{1 - \left(\frac{\hbar c^2 Q}{E_s(\mathbf{Q})}\right)^2}} \right) \tag{1}$$

with a zero-momentum lifetime

$$\widetilde{\tau}_s(0) = \gamma_s^{-1} = \frac{\epsilon_0 A_{uc} \hbar^2 c}{e^2 E_s(0) \mu_{s,\parallel}^2} \tag{2}$$

Thermal averaging of the radiative transition rate $\gamma_s^{\parallel}(\mathbf{Q})$ and inversion gives the averaged lifetime of exciton state s for temperature T[55]

$$\langle \tau_s^{\parallel} \rangle \approx \frac{3}{4} \widetilde{\tau}_s(0) \frac{2 M_s c^2}{E_s^2(0)} k_{\mathrm{B}} T \tag{3}$$

These expressions assume a quadratic exciton dispersion, $E_s(Q) = E_s(0) + \frac{\hbar^2 Q^2}{2 M_s}$. The necessary ingredients, the zero-momentum exciton binding energies $E_s(0)$, the effective exciton mass $M_s = m_e^{*,s} + m_h^{*,s}$, and the transition dipole $\mu_{s,\parallel}^2 = \frac{\hbar^2}{N_k} |\langle \psi_0 | \mathbf{r}^{\parallel} | \psi_s \rangle|^2$ can be directly obtained from the GW band structures and solution of the BSE. N_k is the total number of k points in the grid used for the solution of the BSE. For AB stacking, Equation (3) is not applicable, as the recombination of interlayer excitons should not couple to parallel polarized light. We, hence, followed the approach used by Palummo et al.[55] to arrive at the following expressions of the momentum-dependent recombination rate and the thermally averaged lifetime for perpendicular polarized light

$$\gamma_s^{\perp}(Q) = \frac{E_s(0)}{2\hbar c} \widetilde{\tau}_s^{-1}(0) \cdot \frac{Q^2}{Q_0^3 \sqrt{1 - \frac{Q^2}{Q_0^2}}}$$

$$\langle \tau_s^{\perp} \rangle \approx \frac{3}{2} \widetilde{\tau}_s(0) \frac{2 M_s c^2}{E_s^2(0)} k_{\mathrm{B}} T \tag{4}$$

Table 1 shows the calculated lifetimes for MoSe$_2$/WSe$_2$ heterostructures with three different stacking orders. The effective masses of the valence and conduction bands at K are only weakly dependent on the stacking order and do not significantly affect

Table 1. Averaged radiative lifetimes of inter- and intralayer excitons in MoSe$_2$/WSe$_2$ heterostructures with different stacking orders for a temperature of 4 K ($\langle \tau \rangle$) calculated using Equation (3) and (4) and the excitonic energies and wave functions from our BSE simulations. ILX indicates the lowest-energy "bright" interlayer exciton (X_0) for AA and AB stacking; for AA′ stacking, lifetimes for both the dark X_0 and the bright Y_0 are given. All interlayer exciton lifetimes correspond to emission with light polarization parallel to the plane ($\langle \tau_s^{\parallel} \rangle$), except for AB stacking, where emission of out-of-plane polarized light is predominant ($\langle \tau_s^{\perp} \rangle$).

Exciton	Lifetimes	Stacking order		
		AA	AA′	AB
ILX	$\widetilde{\tau}_s(0)$	65.1 ps	0.34 ns (X_0)	737.6 ps (X_0)
			31.6 ps (Y_0)	
	$\langle \tau_s^{\parallel} \rangle$	10.5 ns	53.8 ns (X_0)	–
			5.34 ns (Y_0)	
	$\langle \tau_s^{\perp} \rangle$	–	–	213.2 ns (X_0)
Mo$_A$	$\widetilde{\tau}_s(0)$	0.34 ps	0.37 ps	0.41 ps
	$\langle \tau_s^{\parallel} \rangle$	46.3 ps	50.6 ps	57.2 ps
W$_A$	$\widetilde{\tau}_s(0)$	0.30 ps	0.34 ps	0.35 ps
	$\langle \tau_s^{\parallel} \rangle$	25.1 ps	29.5 ps	29.0 ps

the predicted lifetimes. For the intralayer excitons, the calculated optical oscillator strength decreases along the sequence AA′→AA→AB, which, according to Equation (3) and (4), causes a corresponding increase of the predicted radiative lifetimes. As expected from experimental data,[36,43,77–79] the lifetimes of the interlayer excitons are predicted to be in the nanosecond range even for very low temperatures and, thus, significantly larger than those of the intralayer excitons. The stacking order has a marked effect on the predicted radiative lifetimes. For AA′ stacking, our calculated zero-momentum lifetime $\widetilde{\tau}_s(0)$ is approximately half the value reported recently from simulations using a combined Dirac–Bloch and gap equations approach[80] and substantially larger (by a factor of 3) than those reported for a bilayer MoSe$_2$/WSe$_2$ heterostructure by Palummo et al.[55] In the AA-stacked heterostructure, the lifetime of the bright X_0 transition is more than twice as long as that of the Y_0 transition for AA′ stacking. These differences might be related to different absolute magnitudes of the optical oscillator strengths. Due to the low oscillator strength even for perpendicular polarized light, we predict the zero-momentum interlayer excitons for AB stacking to be extremely long-lived in terms of radiative decay time, on the order of microseconds; correspondingly, we expect nonradiative decay channels to be prevalent for interlayer excitons in AB-stacked MoSe$_2$/WSe$_2$ heterostructures.

2.4. Momentum-Indirect Interlayer Excitons in TMDC Heterostructures

We will now turn toward the possible contribution of excitons with nonvanishing center-of-mass momentum, for example, transitions related to the fundamental indirect bandgap of TMDC heterostructures, to the "interlayer" peaks observed in PL experiments. Such an indirect transition has been proposed recently to be the origin of the prominent peak at 1.6 eV observed for lattice-incommensurate MoS$_2$/WSe$_2$ heterostructures, in this case, between the valence band maximum at the Γ point of the heterostructure and the local minimum related to the K point of the MoS$_2$ sublayer.[34] An additional feature, which we attributed to the (momentum-indirect) $K^{\mathrm{WSe}_2} \rightarrow K^{\mathrm{MoS}_2}$ transition, was observed at an energy of about 1 eV, in excellent agreement with theoretical simulations of the expected peak position.[35]

A simple and computationally efficient way to estimate the binding energies of excitons with nonzero center-of-mass momentum was proposed recently by Kunstmann et al., who used a four-band tight binding model together with input from DFT calculations to compare the predicted exciton peak positions in MoS$_2$/WSe$_2$ heterostructures with PL measurements.[34] The resulting estimated binding energies of the "momentum-direct" $K \rightarrow K$ exciton and the three "momentum-indirect" $K \rightarrow Q$, $\Gamma \rightarrow Q$, and $\Gamma \rightarrow K$ excitons, as well as the predicted peak positions, are given in **Table 2** for a MoSe$_2$/WSe$_2$ heterostructure with AA′ stacking order (refer to Section 2, Supporting Information, for the input parameters to the tight-binding model extracted from our GW calculations). The model appears to give an estimate of the exciton binding energy of the $K \rightarrow K$ exciton that is in very good agreement with the BSE results, albeit at much lower computational cost. On the other hand, the model suggests that all three considered "momentum-indirect" excitons

Table 2. Calculated binding energies and predicted peak positions of various momentum-direct and momentum-indirect excitons in AA′-stacked $MoSe_2/WSe_2$ heterobilayers from use of a simple tight-binding model[34] and explicit solution of the Bethe–Salpeter equation. For the intralayer and momentum-direct interlayer excitons (K^v–K^c), the values correspond to the lowest-energy optically active transitions; otherwise, the lowest-energy exciton for a particular momentum transfer is listed. The corresponding electronic bandgaps are the transition energies without inclusion of electron–hole interaction effects and can be directly derived from the calculated electronic band structures plotted in Figure 6. All values are given in units of eV.

	Intralayer $MoSe_2$	Intralayer WSe_2	K^v–K^c	K^v–K'^c	K^v–Q^c	Γ^v–Q^c	Γ^v–K^c
Electronic bandgap	1.98	1.97	1.71	1.69	1.51	1.69	1.87
Exciton binding energy (model)	0.41	0.36	0.24	0.24	0.35	0.52	0.62
Exciton binding energy (BSE)	0.31[a]	0.28[a]	0.25[a]	0.23[b]	0.22[b]	0.29[b]	0.25[b]
Peak position model	1.57	1.61	1.48	1.45	1.16	1.17	1.25
BSE	1.67	1.7	1.47	1.46	1.29	1.4	1.62

[a]$33 \times 33 \times 1$ k-point grid without spin–orbit coupling; [b]$36 \times 36 \times 1$ k-point grid without spin-orbit coupling.

have binding energies similar to or larger than those of the intralayer excitons, which is expected to shift the $K \rightarrow Q$ and $\Gamma \rightarrow Q$ peaks below the experimentally observed peak positions. The predicted peak position of the $\Gamma \rightarrow K$ transition is in somewhat better agreement. However, the different valence and conduction band extrema enter the model purely through their effective masses, band offsets, and interlayer coupling parameters. Furthermore, the dielectric screening entering the model is purely local and, thus, contains momentum-dependent screening effects only in an averaged way.

The Bethe–Salpeter equation should be a more accurate and consistent approach, which also explicitly considers nonlocal interaction effects. However, the typical implementations of the BSE in solid-state codes are aimed at the simulation of optical absorption spectra, and hence, only include contributions with vanishing center-of-mass momentum ($\mathbf{Q} = \mathbf{0}^+$). We, hence, extended the widely used YAMBO code[81] to solve the more general Bethe–Salpeter equation[82]

$$(\epsilon_{c,\mathbf{k}+\mathbf{Q}} - \epsilon_{v,\mathbf{k}})A^S_{vc\mathbf{kQ}} + \sum_{v'c'\mathbf{k}'}\langle vc\mathbf{k}+\mathbf{Q}|K^d + K^x|v'c'\mathbf{k}'\rangle$$
$$= E^S_{\mathbf{Q}}A^S_{vc\mathbf{kQ}}$$

(5)

for a finite exciton center-of-mass momentum $\mathbf{Q}$. The band energies $\epsilon_n\mathbf{k}$ are typically quasiparticle energies obtained from G_0W_0 calculations. The exchange kernel

$$\langle vc\mathbf{k}+\mathbf{Q}|K^x|v'c'\mathbf{k}'\rangle = \sum_{\mathbf{G},\mathbf{G}'}\rho_{cv}(\mathbf{k}+\mathbf{Q},\mathbf{Q},\mathbf{G})v_{\mathbf{Q}-\mathbf{G}}$$
$$\times \rho^*_{cv'}(\mathbf{k}'+\mathbf{Q},\mathbf{Q},\mathbf{G}')$$

(6)

couples spin-conserving transitions, whereas the "direct" kernel

$$\langle vc\mathbf{k}+\mathbf{Q}|K^d|v'c'\mathbf{k}'\rangle = \sum_{\mathbf{G},\mathbf{G}'}\rho_{cc'}(\mathbf{k}+\mathbf{Q},\mathbf{q},\mathbf{G})W_{\mathbf{GG}'}(\mathbf{q})$$
$$\times \rho^*_{vv'}(\mathbf{k},\mathbf{q},\mathbf{G}')$$

(7)

determines the formation of bound electron–hole pairs. Here, v is the bare Coulomb interaction, $W_{\mathbf{GG}'}(\mathbf{q}) = \epsilon^{-1}_{\mathbf{GG}'}(\mathbf{q})\sqrt{v(\mathbf{q}+\mathbf{G})}\sqrt{v(\mathbf{q}+\mathbf{G}')}$ is the screened Coulomb interaction, $\rho_{nn'}(\mathbf{k},\mathbf{q},\mathbf{G}) = \langle n\mathbf{k}|e^{-i\mathbf{G}\cdot\mathbf{r}}|n'\mathbf{k}-\mathbf{q}\rangle$ are form factors of the underlying interband transitions, and $\mathbf{q} = \mathbf{k} - \mathbf{k}'$ is a transferred momentum. The typical implementation of the BSE in most solid-state physics codes is recovered by setting $\mathbf{Q}=0$.

To ensure meaningful quantitative results, we solved Equation (5) using a grid of $36 \times 36 \times 1$ k points, neglecting effects from SOI. The obtained exciton binding energies are reported in Table 2. In stark contrast to the model calculations, the BSE predicts the binding energies of the excitons related to indirect electronic transitions in the $MoSe_2/WSe_2$ heterostructure to have very similar magnitudes as those of the $K \rightarrow K$ exciton, in the range of 0.2–0.3 eV. We now find that a possible peak from the $\Gamma \rightarrow K$ transition should be expected close to the intralayer excitonic peaks, suggesting that $\Gamma \rightarrow K$ indeed should not contribute to the interlayer excitonic peak at lower energies. On the other hand, the peak energies of both the $\Gamma \rightarrow Q$ and $K \rightarrow Q$ excitons are predicted to be quite close to those of the $K \rightarrow K$ exciton. As both excitons involve the Q-point conduction band minimum, inclusion of SOI should give rise to two peaks that are split by an energy of about 35 meV in both cases, in agreement with the recently reported experimental observation of momentum-indirect interlayer excitons.[47]
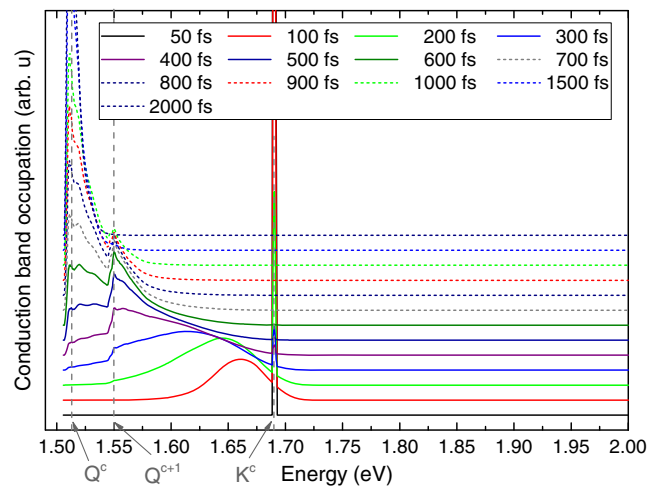
An advantage of the BSE is the access to the exciton wave functions for each predicted excitonic state in the system, in addition to the peak positions and exciton binding energies. **Figure 8** shows the calculated electron and hole parts of the excitonic wave functions of the three considered "indirect" excitons. Based on the electronic band structures shown in Figure 6, one would expect that interlayer excitons have a much weaker layer confinement, and thus spatial separation, of the bound electrons and holes if Γ or Q points are involved, due to the significant interlayer hybridization effects at these points in the Brillouin zone. Our calculations suggest that this assumption is indeed true for the hole part of the exciton wave function: For a hole located at the K point of the Brillouin zone, the corresponding wave function is confined to the WSe_2 layer, whereas for a hole located at the Γ point, the corresponding wave function has a strong interlayer nature with approximately equal weight on the two layers. This suggests that excitons involving Γ-point holes should exhibit characteristically small exciton dipoles compared with the "momentum-direct" $K \rightarrow K$ or $K \rightarrow K'$ excitons that exhibit a distinct interlayer charge separation. For excitons involving the Q-point conduction band valley, the electron part of the exciton wave functions exhibits a small spilling of the electron into the WSe_2 layer, whereas the larger part of the wave function is located in the $MoSe_2$ layer. Based on an integration of the in-plane averaged electron part of the exciton wave function along the out-of-plane direction, we estimate this spillover to be about 30% of the electron wave function if SOI is neglected. This coincides well with the relative contribution of electronic orbitals in the WSe_2 layers to the Q conduction band valley (29%, without
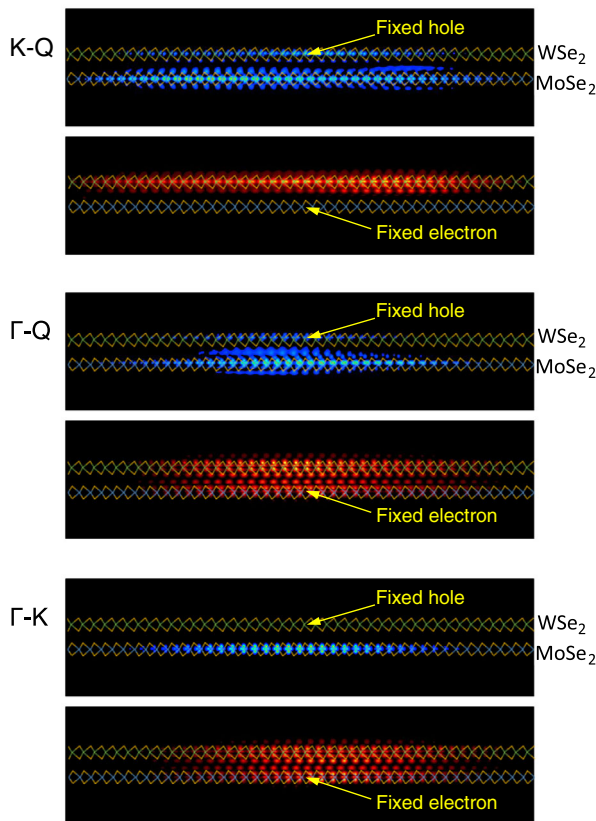
Figure 8. Excitonic wave functions of various momentum-indirect excitons in AA′-stacked MoSe$_2$/WSe$_2$ heterostructures, divided into electron (red density) and hole (blue density) contributions.

Figure 9. Time evolution of the conduction band occupation of an AA′-stacked MoSe$_2$/WSe$_2$ heterostructure under the effect of electron–phonon scattering after an initial placement of 0.1 electrons in the MoSe$_2$-dominated conduction band minimum at each of the K and K' points (K^c) and a temperature of 10 K. The diagram shows the energy-resolved evolution at selected points in time after the initial placement of the charge. Contour plots of snapshots of the k-resolved sum of the band occupations over the Brillouin zone can be found in Section 5, Supporting Information.

SOI), which we estimated using the same method for the Kohn–Sham orbital of the conduction band minimum obtained from DFT. In general, the degree of charge separation for momentum-indirect interlayer excitons should depend significantly on the local stacking order: For an AA stacking order, which we expect to constitute the lowest limit in terms of interlayer hybridization, the contribution of the WSe$_2$ layer to the DFT wave function of the Q valley conduction band minimum is reduced to 16% (without SOI). We note that inclusion of SOI further increases the WSe$_2$ layer weight to the DFT orbitals to 29% for AA stacking and 40% for AA′ stacking, respectively, in good agreement with the composition shown in Figure 6.

Clearly, an additional distinguishing factor between the "direct" $K \rightarrow K$ and the "indirect" $K \rightarrow Q$ and $\Gamma \rightarrow Q$ excitons should be their temperature dependence, as the momentum-indirect excitons require the assistance of momentum sources for their formation and radiative recombination. In typical experiments, the excitation laser energy is too small for appreciable optical excitation at the Γ and Q points and instead optically excites electrons at the K and K' points. To obtain some insight into the scattering dynamics of optically excited electrons and the relevant timescales, we used the Boltzmann transport equation (BTE) as implemented in the PERTURBO code[83] to calculate the time evolution of the conduction band occupations of an AA′-stacked MoSe$_2$/WSe$_2$ under the influence of electron–phonon

coupling.[84] Selected snapshots of the energy-resolved conduction band occupation for a temperature of $T = 10$ K are shown in **Figure 9**. Our calculations suggest that, neglecting the Coulomb interaction between electrons and holes, the electronic charge is efficiently scattered away from the K/K' minima into the conduction band valley around the Q point by phonons with momenta slight smaller than $\overline{KQ}$ within several 100 fs. We find a similar thermalization timescale if the initial charge is placed into the higher energy conduction bands at the K/K' points that are contributed by the WSe$_2$ layer (see Section 4, Supporting Information). Due to the similar exciton binding energies, it would be a reasonable conclusion from these results that there should be a significant population of the global conduction band minimum at the Q point even at low temperatures and, thus, of the lowest-energy excitons over the fundamental bandgap, competing with radiative recombination of $\mathbf{Q} \approx 0$ excitons at the K/K' points of the heterostructure.

On the other hand, both recent magneto-optical experiments[48–50] and theoretical studies[85] suggest that the shift of interlayer exciton binding peak positions under external magnetic fields is a substantial factor for establishing the nature of the contributions to the interlayer excitonic peaks. It was found from magnetoluminescence measurements and similar techniques that the interlayer excitons of MoSe$_2$/WSe$_2$ heterostructures exhibit g-factors that 1) substantially differ from the g-factors of intralayer excitons in the monolayer TMDC materials (usually $|g| \approx 4$) and 2) show a strong dependence on the stacking order: While, for heterostructures in the R registry (e.g., the AA and AB stacking orders in the convention used in this article), g-factors between 4.2 and 8.5 were found,[48] the interlayer exciton g-factors of heterostructures in the H registry are substantially higher, 15–16 for the energetically lowest contribution.[49,50]

Based on theoretical results from density functional theory calculations, the interlayer excitons have, thus, been interpreted to be zero-momentum singlet and triplet excitations at the K and K' points.

The g-factor of a band transition between a valence band state v with crystal momentum $\mathbf{k}$ and a conduction band state c at $\mathbf{k}'$ can be calculated from the relation[86,87]

$$g_{v\mathbf{k},c\mathbf{k}'}^{\text{band}} = m_{c\mathbf{k}'}^z - m_{v\mathbf{k}}^z \tag{8}$$

with the band magnetic moments (in units of μ_B) of valence and conduction bands

$$m_{n\mathbf{k}}^z = m_{n\mathbf{k}}^{\text{orb},z} + m_{n\mathbf{k}}^{\text{spin},z} \tag{9}$$

Here, $m_{n\mathbf{k}}^{\text{spin},z}$ is the expectation value of spin momentum operator in out-of-plane direction $m_{n\mathbf{k}}^{\text{spin},z} = -\frac{e g_e}{2 m_e \mu_B} \langle \Psi_{n\mathbf{k}} | \hat{S}_z | \Psi_{n\mathbf{k}} \rangle$, with spinor wave functions $\Psi_{n\mathbf{k}}$. $m_{n\mathbf{k}}^{\text{orb}}$ is the corresponding orbital contribution to the magnetic moment and for a magnetic field in the z-direction is given by the relation[88]

$$m_{n\mathbf{k}}^{\text{orb},z} = -\frac{i}{m_e \mu_B} \sum_{j \neq n} \left(\frac{\langle \Psi_{n\mathbf{k}} | \hat{\pi}_x | \Psi_{j\mathbf{k}} \rangle \langle \Psi_{j\mathbf{k}} | \hat{\pi}_y | \Psi_{n\mathbf{k}} \rangle}{E_{j\mathbf{k}} - E_{n\mathbf{k}}} - \frac{\langle \Psi_{n\mathbf{k}} | \hat{\pi}_y | \Psi_{j\mathbf{k}} \rangle \langle \Psi_{j\mathbf{k}} | \hat{\pi}_x | \Psi_{n\mathbf{k}} \rangle}{E_{j\mathbf{k}} - E_{n\mathbf{k}}} \right) \tag{10}$$

where π is given by the momentum operator plus possible contributions from spin–orbit coupling.[85] Both m_{nk}^{orb} and m_{nk}^{spin} can be extracted in a straightforward way from density functional theory calculations.

Within the typically implemented excitonic Bethe–Salpeter equation formalism, the exciton is described by a weighted superposition of different interband transitions. With this, one can define an effective g-factor for an excitonic state S with center-of-mass momentum $\mathbf{Q}$ by

$$g_{S,\mathbf{Q}}^{\text{exc}} = 2 \sum_{v,c,\mathbf{k}} A_{vck}^{S,\mathbf{Q}} g_{v\mathbf{k},c\mathbf{k}+\mathbf{Q}}^{\text{bands}} \tag{11}$$

where the excitonic wave function $A_{v\mathbf{k},c\mathbf{k}'}$ describes the weight of each transition contributing to the exciton. Depending on the exciton in question, the mixing of different transitions in the BSE approach might, thus, lead to somewhat different g^{exc} compared with g^{band} for a given excitonic transition. For instance, Deilmann et al. reported recently[86] that even for the A excitons of monolayer TMDCs, which are very localized in reciprocal space and consist to more than 95% of a $v \to c$ transition at the K/K' points, the additional small contributions can lower g_A^{exc} compared with g_{cvK}^{band} by about 30%.

Table 3 shows the calculated effective exciton g-factors g^{exc} and band approximations g^{band} for selected momentum-direct and -indirect excitons of an AA'-stacked $MoSe_2/WSe_2$ heterostructure.[89] Plots of the underlying magnetic moments of valence and conduction bands and of the spin contribution for AA and AA' stackings are shown in **Figure 10**. Our calculated values for g^{band} are in reasonable agreement with previous theoretical studies and the experimental data and support the assignment of the interlayer excitons to a pair of momentum-direct singlet and triplet excitations at the K and K' points. While the g-factors of the energetically lowest $K \to Q$ transitions show a certain dependence on the stacking order, this dependence appears to originate in changes in interband hybridization at the Q point. The induced variation of the g-factors and energetic order of the exciton with the higher and the exciton with the lower g-factor are not consistent with the available experimental data. A similar

Table 3. Calculated g-factor for selected momentum-direct and -indirect excitons. g_{exc} and g_{band} are the effective exciton g-factor as calculated from the excitonic wave functions and the g-factors in the two-bands approximation, respectively. Upper indices indicate the method used to calculate the interband transition energies entering Section 2.4. All values are in units of μ_B.

		$K^v \to K^c$	$K^v \to K^{c+1}$	$K^v \to K'^c$	$K^v \to Q^c$	$K^v \to Q^{c+1}$	$\Gamma^v \to K^c$	$\Gamma^v \to Q^c$
AA	$g_{\text{band}}^{\text{DFT}}$	-5.95 ($\uparrow\uparrow$)	-10.45 ($\uparrow\downarrow$)	-16.88 ($\uparrow\downarrow$)	-8.41 ($\uparrow\uparrow$)	-12.16 ($\uparrow\downarrow$)	7.14 ($-\uparrow$)	4.68 ($-\uparrow$)
	$g_{\text{exc}}^{\text{DFT}}$	-5.89	-10.38	-16.80				
	$g_{\text{exc}}^{\text{GW}}$	-5.00	-9.27	-13.88				
	Exp	-8.5[a] -5.5 ± 0.8[b]						
AA'	$g_{\text{band}}^{\text{DFT}}$	-16.48 ($\uparrow\downarrow$)	-12.01 ($\uparrow\uparrow$)	-5.65 ($\uparrow\uparrow$)	-9.15 ($\uparrow\uparrow$)	-12.98 ($\uparrow\downarrow$)	-6.94 ($-\uparrow$)	0.4 ($-\uparrow$)
	$g_{\text{exc}}^{\text{DFT}}$	-16.47[c]	-12.01[c]	-5.65[c]	-9.14[c]	-12.82[c]	-5.34[c]	-3.76[c]
		-16.34	-11.87	5.55				
	$g_{\text{exc}}^{\text{GW}}$	-13.67[c]	-9.41[c]	-4.83[c]	-7.39[c]	-11.00[c]	-4.35[c]	-3.45[c]
		-13.58	-9.31	4.75				
	Exp	15.2[d], -16[e]	10.7[d]					
AB	$g_{\text{band}}^{\text{DFT}}$	-5.91 ($\uparrow\uparrow$)	-10.43 ($\uparrow\downarrow$)	-16.88 ($\uparrow\downarrow$)	-8.11 ($\uparrow\uparrow$)	-11.76 ($\uparrow\downarrow$)	6.10 ($-\uparrow$)	3.90 ($-\uparrow$)
	$g_{\text{exc}}^{\text{DFT}}$	-5.81	-10.30	-16.74				
	$g_{\text{exc}}^{\text{GW}}$	-4.96	-9.23	-13.88				
	Exp	7.1[f]						

[a]Ref. [48]; [b]Ref. [49]; [c]12 × 12 × 1 k-point grid; [d]Ref. [49], signs of g-factor not reported; [e]Ref. [50]; [f]Ref. [48].
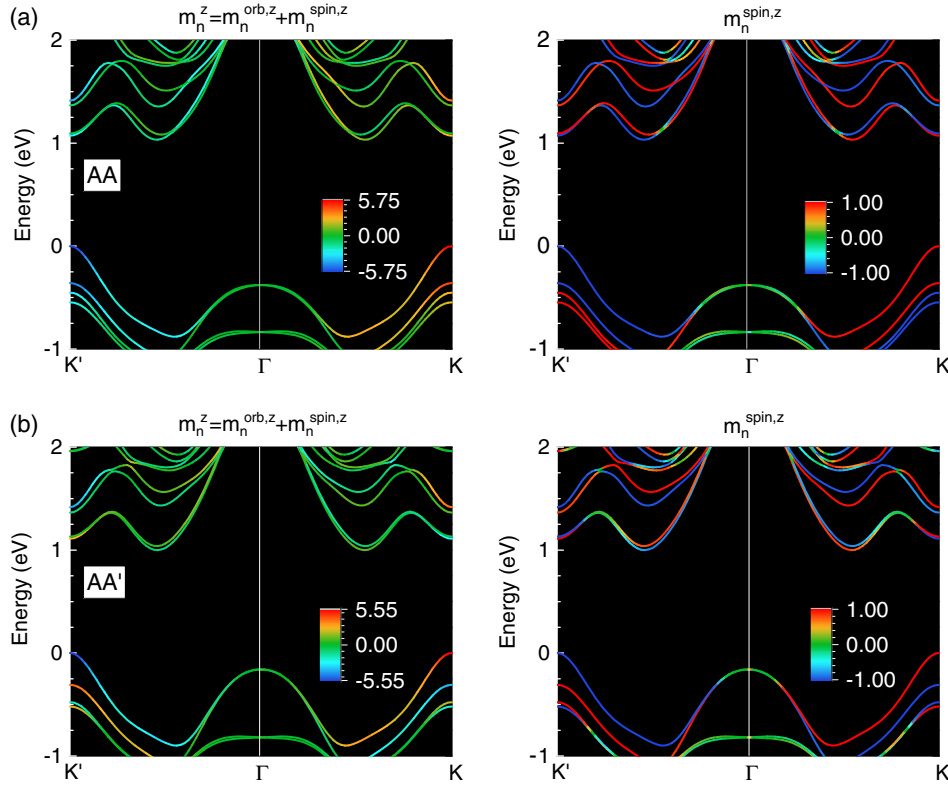
Figure 10. Left side: Calculated band magnetic moments (in units of μ_B) of valence and conduction bands of MoSe$_2$/WSe$_2$ with a) AA and b) AA$'$ stacking order. Right side: Spin contributions to the band magnetic moments.

conclusion can be reached for the other momentum indirect excitons.

As expected from the previous reported results for the excitonic g-factors of the monolayer materials,[86] the inclusion of excitonic effects modifies the calculated effective g-factors of the MoSe$_2$/WSe$_2$ heterostructure. For the $K \rightarrow K$ transitions and using the DFT band energies for the calculation of m^{orb}, the calculated g^{exc} values are about 1% smaller than the corresponding g^{band} values, which validates the band approximation for description of the momentum-direct K interlayer excitons. We note that when using a coarser 12×12 k-point grid for the solution of the BSE, the difference to g^{band} is even smaller, due to the larger weight put on contributions at the K and K' points in this case. The contributions to the indirect excitons are less localized in reciprocal space compared with the momentum-direct interlayer excitons, and the differences between g^{exc} and g^{band} are larger in this case. A further change appears if we use GW band energies for the calculation of m^{orb}: due to the larger energy differences, the calculated g-factors are substantially smaller than those calculated from DFT-level band energies. This somewhat decreases the agreement between the experimental data and the predicted g-factors for the $K \rightarrow K$ excitons. The discrepancy might arise from the neglect of substrate and environmental effects in the simulations, affecting both the electronic band energies in the material and somewhat delocalizing the excitonic wave functions due to screening effects compared with the "freestanding" material in vacuum. Another possible source of discrepancy is the use of DFT spinors for the calculation of the orbital magnetic moments, which is not fully consistent with the use of G_0WW_0 transition energies.

As an alternative to the interpretation of the doublet structure of the interlayer PL peak as a pair of charge-neutral excitons, Calman et al.[40] have recently suggested a pair of spatially indirect neutral exciton and spatially indirect negatively charged trion as the origin. A formalism for the estimation of the effective g-factor of trions was proposed and used by Lyons et al. for the interpretation of the trion valley Zeeman splitting in monolayer WSe$_2$.[90] For a specific negatively charged trion configuration defined by the valley indices τ (+1 for the K-point valleys, -1 for the K'-point valleys), the Zeeman splitting can be expressed through the relation

$$\Delta E = g_T \mu_B B_z = \frac{1}{2}(\tau_{exc}g_{exc} - \tau_c g_e - 2g_l)\mu_B B_z \tag{12}$$

where g_T is the trion effective g-factor due to valley- and spin-induced magnetic momenta, and g_{exc} and $g_e = 2m_c^z$ are the exciton effective g-factor of the recombining electron–hole pair and the g-factor of an excess electron in a specific MoSe$_2$-dominated conduction band valley, respectively. The effect of the recoil of the excess electron after recombination of the electron–hole pair on the Zeeman splitting is included through a Landau-level-associated g-factor $g_l = 2m_X^*/(m_c^*m_T^*)$. Here, m_e^* is the effective mass of the excess electron, $m_X^* = m_v^* + m_c^*$ is the exciton effective mass, and $m_T^* = m_X^* + m_e$ is the trion effective mass. We

derived the effective masses of the valence band maximum and the spin–orbit split conduction band valley from our calculated DFT band structures (see Section 2, Supporting Information). This results in g_l in the range of 1.8–2.2 for all considered trion configurations, very similar to the experimentally deducted value in monolayer WSe_2.[90]

Based on Equation (12), we calculated the trion effective g-factors g_T for the three trion configurations shown in Figure 10 for the case of an AA′-stacked heterostructure. All three considered interlayer trion configurations consist of the bright neutral interlayer exciton Y_0 and an excess electron in different conduction band valleys and have been predicted to occur in the optical absorption spectra of vertically stacked MoS_2/WS_2.[58] The trion binding energies of 25–28 meV relative to the neutral interlayer exciton obtained in the previous studies[58] for the MoS_2/WS_2 heterostructure are similar to the trion binding energies predicted for TMDC monolayers.[91] Under the assumption of a similar binding energy in $MoSe_2/WSe_2$ heterostructures, all three trion configurations would give rise to absorption/emission peaks close to the "darkish" X_0 interlayer exciton. Our results suggest that the three configurations should exhibit characteristic g-factors in the range of 5–11, distinctively different from the g-factor of 16.5 predicted for the X_0 interlayer exciton.

Finally, we note that, in principle, the exchange interaction between the three bound particles in the spin-triplet trion configuration shown in **Figure 11**b should give rise to an exchange-induced Berry curvature Ω_{ex},[90,92] inducing an additional magnetic momentum and a g-factor contribution $g_{BP} = \frac{m_0}{2\hbar^2} \delta_{exch}\Omega_{ex}(\mathbf{k} = \mathbf{K})$[90] ($\delta_{ex}$ is the exchange splitting and m_0 is the free electron rest mass). For monolayer WSe_2, this g-factor contribution has been estimated to be about $g_{BP} = 4$, i.e., rather sizeable.[90,92] However, due to the significant charge separation of electrons and holes in the case of the $K \rightarrow K$ interlayer excitons and the associated trions, and thus the marginal spatial overlap between the electron and hole wave functions (about 1/1000th of the spatial overlap of the electron and hole wave functions of the Mo_A and W_A intralayer excitons), we estimate the g-factor contribution induced by electron–hole exchange to be negligibly small compared with the situation in the monolayer materials.
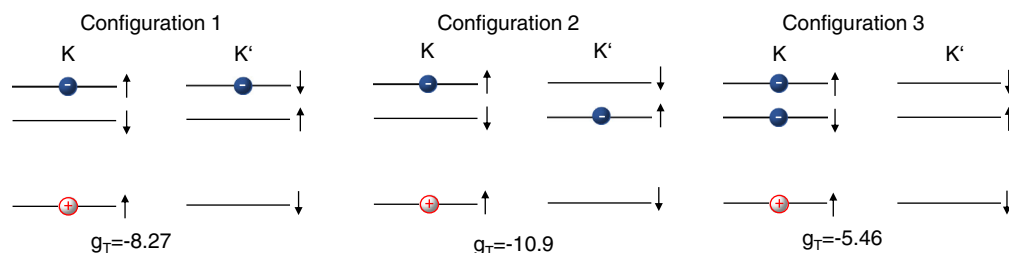
2.5. C-Type Excitons in AA′-Stacked $MoSe_2/WSe_2$ Heterostructures

In this section, we will go beyond the excitons around the absorption onset and consider the composition of the optical absorption at slightly larger energies. As shown in Section 2.2, the absorption spectra of monolayer molybdenum- and tungsten-based TMDCs feature strongly bound "C" excitons, which arise from a high joint-density-of-states between valence and conduction bands. The fulfillment of these band nesting conditions depends on details in the electronic structure. At the same time, the electronic contribution to the wave function of the monolayer C excitons features a noticeable component that points in out-of-plane direction, which we found gave rise to a significant spatial interlayer delocalization of the excitonic wave functions for TMDC homobi- and trilayers. An interesting question is then how the tightly bound C excitons are affected by the formation of a heterostructure.

The calculated optical spectrum of an AA′-stacked $MoSe_2/WSe_2$ heterostructure shows a number of peaks with higher oscillator strength in the energy range of 2.0–2.5 eV, where the C excitons of monolayer $MoSe_2$ and WSe_2 are located. In the following, we will focus on four of these bright transitions, as labeled in **Figure 12**. These states have in common that their k-resolved excitonic wave functions, i.e., the location of the band transitions contributing to the excitonic state in the Brillouin zone of the material, are very similar to those of the C excitons in monolayer $MoSe_2$ and WSe_2. **Figure 13** shows the calculated k-resolved exciton wave functions. In all four cases, the strongest contributions come from the direct vicinities of the K and K′ points, with additional contributions from a "special" point on the $Q - K/K'$ lines. As for the monolayer materials, the location of this special point is given by a band nesting between valence and conduction bands, which appears to be present in the slightly modified electronic band structure of the heterostructure as well. This suggests that all four selected absorption peaks are "C-like".

As the plots of the real-space excitonic wave functions in **Figure 14** show, we can divide the four selected transitions into two groups: Two transitions at lower energies, C_1^{inter} and C_2^{inter}, show a distinct interlayer nature. C_1^{inter} arises from transitions from the WSe_2-dominated valence band into the $MoSe_2$-dominated lowest conduction band, which, interestingly, suggests that the slope of these two bands is sufficiently similar to establish an effective band nesting condition even between bands contributed by different materials. The corresponding excitonic wave function shows a clear confinement of the hole part to the WSe_2 layer, whereas the electron part is mostly located in the $MoSe_2$ layer, but spills over into neighboring WSe_2 layer, similar to the exciton wave function in $MoSe_2$ homobilayers. The

Figure 11. Electron and hole configurations of three selected negatively charged trions associated with the "bright" interlayer exciton Y_0 in an AA′-stacked $MoSe_2/WSe_2$ heterostructure. In all cases, a radiatively combining electron–hole pair is located at the K point of the hexagonal Brillouin zone with the excess charge located either in the K or K′ valleys. The calculated effective g-factor g_T is given for each configuration.
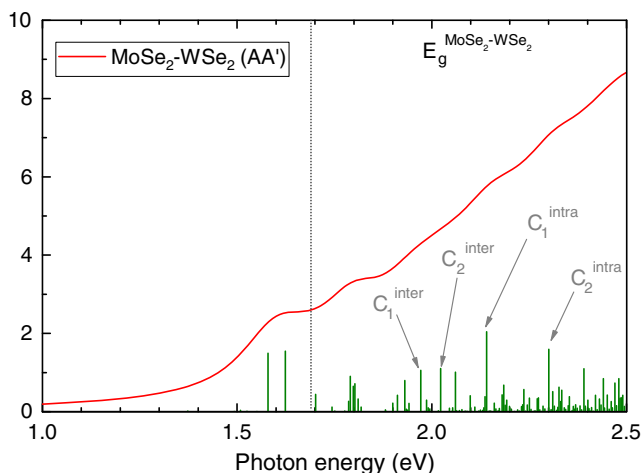
Figure 12. Calculated absorption spectrum of an AA′-stacked $MoSe_2/WSe_2$ heterostructure. The labels indicate the positions of the four selected C-type excitons discussed in the main text.

electronic part of the exciton wave function shows a bright and localized "core" with some additional density tail from band-like states of similar energy that are mixed into the exciton wave function. This localization is also mirrored in the exciton binding energy: based on the energy difference between the highest valence and the lowest conduction band at the special point, which our calculations indicate to have the largest contribution to the exciton, we estimate the exciton binding energy to be about 453 meV.

The situation is somewhat reversed for C_2^{inter}: here, the largest contributions come from transitions at the K and K' points and

their immediate vicinity, between the second and third highest valence bands (of purely $MoSe_2$ or WSe_2 nature) into the third lowest conduction band, which is contributed by the WSe_2 layer; see the electronic band structure shown in Figure 6. Smaller contributions come from transitions at the band nesting point, between the valence band top and the hybridized second lowest conduction band. Consequently, it is the hole part of the excitonic wave function that shows a distinct interlayer delocalization in this case, with the larger share of the hole being located in the $MoSe_2$ layer, whereas the electronic part is well localized in the WSe_2 and only shows a minor spilling into the neighboring material. Within the layer, the electron appears to be well localized, with an exciton radius of about 35 Å. Based on the energy difference between the initial and final states at the K point and the exciton peak position, we estimate the exciton binding energy to be 448 meV. We can, thus, understand C_1^{inter} and C_2^{inter} as "interlayer C excitons," with a noticeable interlayer separation of bound electrons and holes.

In contrast to the previous two states, the second group of transitions can be more or less clearly be attributed to arise from individual layer and, thus, have a noticeable intralayer nature. C_1^{intra} consists of a mix of almost degenerate $MoSe_2 \rightarrow WSe_2$ transitions close to the K and K' points and additional C-like transitions away from K. Despite this, we find that the exciton wave function has a significant intralayer nature centered on the $MoSe_2$ layer, and the electron part is quite localized. In terms of both spatial distribution and contributions in reciprocal space, C_1^{intra} appears to be analogous to the C excitons in mono- and bilayer $MoSe_2$. From a weighted average of the energies of the transitions contributing to the exciton wave functions, the binding energy is calculated to be 400 meV. The C_2^{intra} transition, on the other hand,
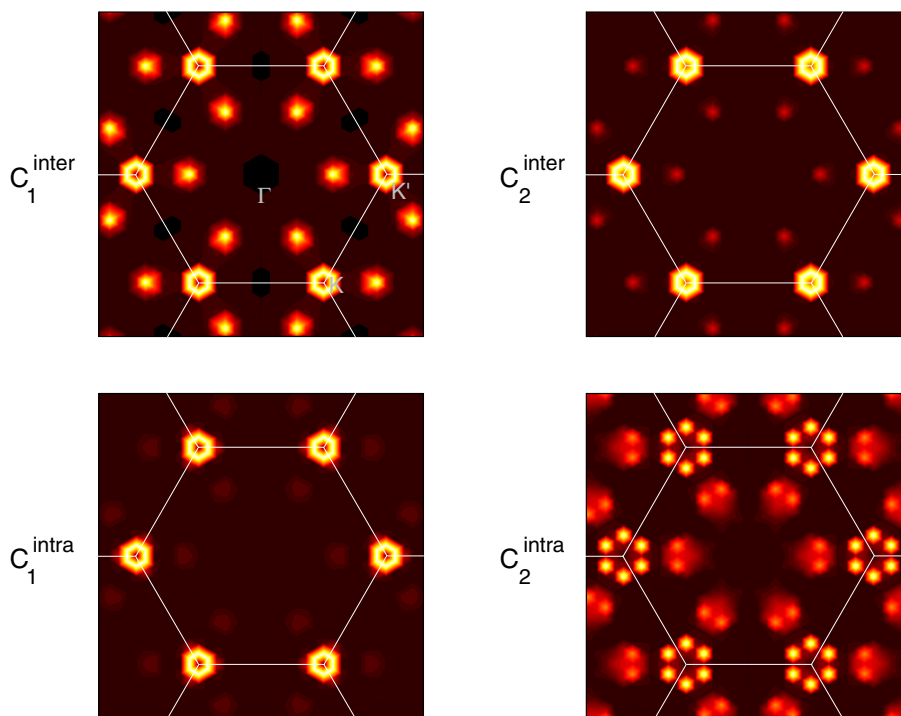
Figure 13. k-resolved representation of the excitonic wave functions of four selected C-type excitons in AA-stacked $MoSe_2/WSe_2$ heterostructures. Brighter colors indicate a larger contribution of direct band transitions at a given point in the Brillouin zone to the excitonic state.

2000614 (15 of 19)
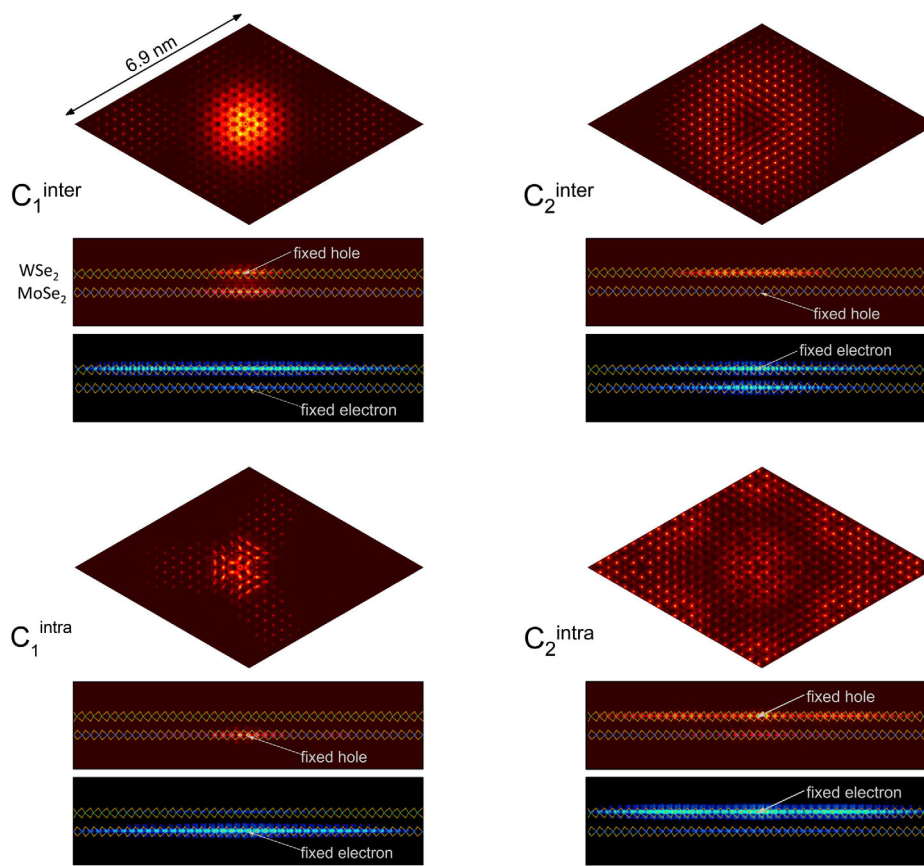
Figure 14. Plots of the electron (red) and hole (blue) parts of the excitonic wave functions of four C-like excitons in an AA′-stacked MoSe$_2$/WSe$_2$ heterostructure. Top parts of the subfigures show projections of the wave function onto the x–y plane, and bottom parts show projections onto the x–z plane.

mainly consists of intralayer transitions within the WSe$_2$ layer and, thus, has some resemblance to the C excitons of WSe$_2$. Quite surprisingly, while the electron and hole parts of the exciton wave function appear to be quite delocalized, we calculate a rather high exciton binding energy of 414 meV from the difference of the peak energy to a weighted average of the energies of the constituting band transitions. It is, thus, possible that the calculated C_2^{intra} peak, in fact, consists of an exciton mixed with band transitions of similar energy, which gives rise to an extended wave function. A more detailed decomposition would be necessary to draw further conclusions on the nature of the C_2^{intra} peak.

3. Conclusion

We have expanded, on our previous study, on the excitonic spectra of vertically stacked MoSe$_2$/WSe$_2$ heterostructures. The previously reported significantly stacking-dependent optical oscillator strengths of the lowest energy interlayer excitons lead to a wide range of radiative lifetimes. In particular, deriving an equation for excitons emitting out-of-plane polarized light, we were able to quantify the radiative lifetime of the "brightish" interlayer excitons in AB-stacked heterostructures to 200 ns (at $T = 4$ K), significantly larger than the lifetimes obtained for

the investigated AA and AA′ stacking orders. We expect these results to be transferable to other stacking orders as well.

By virtue of implementation and solution of the finite-momentum Bethe–Salpeter equation, we further studied the binding energies and wave functions of relevant momentum indirect excitons between the valence and conduction band valleys. Here, we showed from ab initio that the momentum-indirect excitons over the fundamental bandgap ($K \rightarrow Q$) should be the lowest-energy excitons for ideally stacked MoSe$_2$/WSe$_2$ heterostructures, about 0.15 eV below the momentum-direct $K \rightarrow K$ excitations with a significant decrease of spatial charge separation due to interlayer hybridization effects. Experimental observation of such momentum-indirect interlayer excitons has been reported recently by Hanbicki et al.[47] Simulations of the carrier dynamics of free electrons suggest that the global conduction band minimum should be quickly populated after optical excitation in resonance with the intralayer "A" excitons. Despite these results, our calculations of the effective exciton Landé g-factors confirm previous reports that the experimentally observed interlayer exciton magnetoluminescence in bilayer MoSe$_2$/WSe$_2$ heterostructures probably stems from (quasi-)momentum direct $K \rightarrow K$ interlayer excitons. In particular, compared with the TMDC homobilayers and the related MoS$_2$/WS$_2$ heterostructures, this raises the question why the $K \rightarrow Q$ excitons do not appear to be commonly observed in PL measurements of

MoSe$_2$/WSe$_2$ bilayer heterostructures. Future theoretical and experimental work might shed further light on, e.g., the influence of the moiré potential on the interlayer excitonic and trionic spectra.

Analyzing the calculated absorption spectra, we further reveal the existence of higher energy interlayer excitons with a larger delocalization in reciprocal space and high binding energy, which can be interpreted as interlayer analog to the prominent C excitons in TMDCs mono- and few-layer materials.

Supporting Information

Supporting Information is available from the Wiley Online Library or from the author.

Acknowledgements

Conflict of Interest

The author declares no conflict of interest.

Data Availability Statement

Research data are not shared.

Keywords

[1] K. S. Novoselov, A. K. Geim, S. V. Morozov, D. Jiang, Y. Zhang, S. V. Dubonos, I. V Grigorieva, A. A. Firsov, *Science* **2004**, *36*, 666.

[2] K. S. Novoselov, D. Jiang, F. Schedin, T. J. Booth, V. V. Khotkevich, S. V. Morozov, A. K. Geim, *Proc. Natl. Acad. Sci. USA* **2005**, *102*, 10451.

[3] N. Mounet, M. Gibertini, P. Schwaller, D. Campi, A. Merkys, A. Marrazzo, T. Sohier, I. E. Castelli, A. Cepellotti, G. Pizzi, N. Marzari, *Nat. Nanotechnol.* **2018**, *13*, 246.

[4] G. Cheon, E. D. Cubuk, E. R. Antoniuk, L. Blumberg, J. E. Goldberger, E. J. Reed, *J. Phys. Chem. Lett.* **2018**, *9*, 6967.

[5] K. F. Mak, C. Lee, J. Hone, J. Shan, T. F. Heinz, *Phys. Rev. Lett.* **2010**, *105*, 136805.

[6] A. Splendiani, L. Sun, Y. Zhang, T. Li, J. Kim, C.-Y. Chim, G. Galli, F. Wang, *Nano Lett.* **2010**, *10*, 1271.

[7] S. Tongay, J. Suh, C. Ataca, W. Fan, A. Luce, J. S. Kang, J. Liu, C. Ko, R. Raghunathanan, J. Zhou, F. Ogletree, J. Li, J. C. Grossman, J. Wu, *Sci. Rep.* **2013**, *3*, 2657.

[8] H. R. Gutierrez, N. Perea-Lopez, A. L. Elias, A. Berkdemir, B. Wang, R. Lv, F. Lopez-Urias, V. H. Crespi, H. Terrones, M. Terrones, *Nano Lett.* **2012**, *13*, 3447.

[9] S. Mouri, Y. Miyauchi, K. Matsuda, *Nano Lett.* **2013**, *13*, 5944.

[10] N. Scheuschner, O. Ochedowski, A.-M. Kaulitz, R. Gillen, M. Schleberger, J. Maultzsch, *Phys. Rev. B* **2014**, *89*, 125406.

[11] R. Klots, A. K. M. Newaz, B. Wang, D. Prasai, H. Krzyzanowska, J. Lin, D. Caudel, N. J. Ghimire, J. Yan, B. L. Ivanov, K. A. Velizhanin, A. Burger, D. G. Mandrusan, N. H. Tolk, S. T. Pantelides, K. I. Bolotin, *Sci. Rep.* **2014**, *4*, 6608.

[12] K. He, N. Kumar, L. Zhao, Z. Wang, K. F. Mak, H. Zhao, J. Shan, *Phys. Rev. Lett.* **2014**, *113*, 026803.

[13] M. M. Ugeda, A. J. Bradley, S.-F. Shi, F. H. da Jornada, Y. Zhang, D. Y. Qiu, W. Ruan, S.-K. Mo, Z. Hussain, Z.-X. Shen, F. Wang, S. G. Louie, M. F. Crommie, *Nat. Mater.* **2014**, *13*, 1091.

[14] B. Zhu, X. Chen, X. Cui, *Sci. Rep.* **2015**, *5*, 9218.

[15] H. M. Hill, A. F. Rigosi, C. Roquelet, A. Chernikov, T. C. Berkelbach, D. R. Reichman, M. S. Hybertsen, L. E. Brus, T. F. Heinz, *Nano Lett.* **2015**, *15*, 2992.

[16] C. Zhang, Y. Chen, A. Johnson, M.-Y. Li, L.-J. Li, P. C. Mende, R. M. Feenstra, C.-K. Shih, *Nano Lett.* **2015**, *15*, 6494.

[17] A. F. Rigosi, H. M. Hill, K. T. Rim, G. W. Flynn, T. F. Heinz, *Phys. Rev. B* **2016**, *94*, 075440.

[18] G. Wang, A. Chernikov, M. M. Glazov, T. F. Heinz, X. Marie, T. Amand, B. Urbaszek, *Rev. Mod. Phys.* **2018**, *90*, 021001.

[19] M. Goryca, J. Li, A. V. Stier, T. Taniguchi, K. Watanabe, E. Courtade, S. Shree, C. Robert, B. Urbaszek, X. Marie, S. A. Crooker, *Nat. Commun.* **2019**, *10*, 4172.

[20] D. Y. Qiu, F. H. da Jornada, S. G. Louie, *Phys. Rev. Lett.* **2013**, *111*, 216805.

[21] R. Gillen, J. Maultzsch, *IEEE J. Sel. Top. Quantum Electron.* **2017**, *23*, 219.

[22] A. Carvalho, R. M. Ribeiro, A. H. Castro Neto, *Phys. Rev. B* **2013**, *88*, 115205.

[23] S. Lin, X. Li, P. Wang, Z. Xu, S. Zhang, H. Zhong, Z. Wu, W. Xu, H. Chen, *Sci. Rep.* **2015**, *5*, 15103.

[24] F. Withers, O. D. Pozo-Zamudio, A. Mishchenko, A. P. Rooney, A. Gholinia, K. Watanabe, T. Taniguchi, S. J. Haigh, A. K. Geim, A. Tartakovskii I, K. S. Novoselov, *Nat. Mater.* **2015**, *14*, 301.

[25] O. Lopez-Sanchez, D. Lembke, M. Kayci, A. Radenovic, A. Kis, *Nat. Nanotechnol.* **2013**, *8*, 497.

[26] P. Tonndorf, R. Schmidt, R. Schneider, J. Kern, M. Buscema, G. A. Steele, A. Castellanos-Gomez, H. S. J. van der Zant, S. M. de Vasconcellos, R. Bratschitsch, *Optica* **2015**, *4*, 347.

[27] Y.-M. He, G. Clark, J. R. Schaibley, Y. He, M.-C. Chen, Y.-J. Wei, X. Ding, Q. Zhang, W. Yao, X. Xu, C.-Y. Lu, J.-W. Pan, *Nat. Nanotechnol.* **2015**, *10*, 497.

[28] C. Chakraborty, L. Kinnischtzke, K. M. Goodfellow, R. Beams, A. N. Vamivakas, *Nat. Nanotechnol.* **2015**, *10*, 507.

[29] A. Srivastava, M. Sidler, A. V. Allain, D. S. Lembke, A. Kis, A. Imamoğlu, *Nat. Nanotechnol.* **2015**, *10*, 491.

[30] D. Xiao, G.-B. Liu, W. Feng, X. Xu, W. Yao, *Phys. Rev. Lett.* **2012**, *108*, 196802.

[31] O. L. Sanchez, D. Ovchinnikov, S. Misra, A. Allain, A. Kis, *Nano Lett.* **2016**, *16*, 5792.

[32] Y. Yu, S. Hu, L. Su, L. Huang, Y. Liu, Z. Jin, A. A. Purezky, D. B. Geohegan, K. W. Kim, Y. Zhang, L. Cao, *Nano Lett.* **2015**, *15*, 486.

[33] H. Fang, C. Battaglia, C. Carraro, S. Nemsak, B. Ozdol, J. S. Kang, H. A. Bechtel, S. B. Desai, F. Kronast, A. A. Unal, G. Conti, C. Conlon, G. K. Palsson, M. C. Martin, A. M. Minor, C. S. Fadley, E. Yablonovitch, R. Maboudian, A. Javey, *Proc. Natl. Acad. Sci. USA* **2014**, *111*, 6198.

[34] J. Kunstmann, P. N. F. Mooshammer, A. Chaves, N. P. F. Stein, G. Plechinger, C. Strunk, C. Schäller, G. Seifert, D. Reichman, T. Korn, *Nat. Phys.* **2018**, *14*, 801.

[35] O. Karni, E. Barré, S. C. Lau, R. Gillen, E. Y. Ma, B. Kim, K. Watanabe, T. Taniguchi, J. Maultzsch, K. Barmak, R. H. Page, T. F. Heinz, *Phys. Rev. Lett.* **2019**, *123*, 247402.

[36] P. Rivera, J. R. Schaibley, A. M. Jones, J. S. Ross, S. Wu, G. Aivazian, P. Klement, K. Seyler, G. Clark, N. J. Ghimire, J. Yan, D. G. Mandrus, W. Yao, X. Xu, *Nat. Commun.* **2015**, *6*, 6242.

[37] J. S. Ross, P. Rivera, J. Schaibley, E. Lee-Wong, H. Yu, T. Taniguchi, K. Watanabe, J. Yan, D. Mandrus, D. Cobden, W. Yao, X. Xu, *Nano Lett.* **2017**, *17*, 638.

[38] P. K. Nayak, Y. Horbatenko, S. Ahn, G. Kim, J.-U. Lee, K. Y. Ma, A.-R. Jang, H. Lim, D. Kim, S. Ryu, H. Cheong, N. Park, H. S. Shin, *ACS Nano* **2017**, *11*, 4041.

[39] K. Tran, G. Moody, F. Wu, X. Lu, J. Choi, K. Kim, A. Rai, D. A. Sanchez, J. Quan, A. Singh, J. Embley, A. Zepeda, M. Campbell, T. Autry, T. Taniguchi, K. Watanabe, N. Lu, S. K. Banerjee, K. L. Silverman, S. Kim, E. Tutuc, L. Yang, A. H. MacDonald, X. Li, *Nature* **2019**, *567*, 71.

[40] E. V. Calman, L. H. Fowler-Gerace, D. J. Choksy, L. V. Butov, D. E. Nikonov, I. A. Young, S. Hu, A. Mishchenko, A. K. Geim, *Nano Lett.* **2020**, *20*, 1869.

[41] D. Kozawa, A. Carvalho, I. Verzhbitskiy, F. Giustiniano, Y. Miyauchi, S. Mouri, A. H. C. Neto, K. Matsuda, G. Eda, *Nano Lett.* **2016**, *16*, 4087.

[42] F. Ceballos, M. Z. Bellus, H.-Y. Chiu, H. Zhao, *Nanoscale* **2015**, *7*, 17523.

[43] B. Miller, A. Steinhoff, B. Pano, J. Klein, F. Jahnke, A. Holleitner, U. Wurstbauer, *Nano Lett.* **2017**, *17*, 5229.

[44] M. Förg, L. Colombier, R. K. Patel, J. Lindlau, A. D. Mohite, H. Yamaguchi, M. M. Glazov, D. Hunger, A. Högele, *Nat. Commun.* **2019**, *10*, 3697.

[45] J. Kang, S. Tongay, J. Zhou, J. Li, J. Wu, *Appl. Phys. Lett.* **2013**, *102*, 012111.

[46] M. M. Furchi, A. A. Zechmeister, F. Hoeller, S. Wachter, A. Pospischil, T. Mueller, *IEEE J. Sel. Top. Quantum Electron.* **2017**, *23*, 106.

[47] A. T. Hanbicki, H.-J. Chuang, M. R. Rosenberger, C. S. Hellberg, S. V. Sivaram, K. M. McCreary, I. Mazin I, B. T. Jonker, *ACS Nano* **2018**, *12*, 4719.

[48] A. Ciarrocchi, D. Unuchek, A. Avsar, K. Watanabe, T. Taniguchi, A. Kis, *Nat. Photon.* **2019**, *13*, 131.

[49] T. Wang, S. Miao, Z. Li, Y. Meng, Z. Lu, Z. Lian, M. Blei, T. Taniguchi, K. Watanabe, S. Tongay, D. Smirnov, S.-F. Shi, *Nano Lett.* **2020**, *20*, 694.

[50] A. Delhomme, D. Vaclavkova, A. Slobodeniuk, M. Orlita, M. Potemski, D. M. Basko, K. Watanabe, T. Taniguchi, D. Mauro, C. Barreteau, E. Giannini, A. F. Morpurgo, N. Ubrig, C. Faugeras, *2D Mater.* **2020**, *7*, 041002.

[51] M. Förg, A. S. Baimuratov, S. Y. Kruchinin, I. A. Vovk, J. Scherzer, J. Förste, V. Funk, K. Watanabe, T. Taniguchi, A. Högele, *Nat. Commun.* **2021**, *12*, 1656.

[52] M. Okada, A. Kutana, Y. Kureishi, Y. Kobayashi, Y. Saito, T. Saito, K. Watanabe, T. Taniguchi, S. Gupta, Y. Miyata, B. I. Yakobson, H. Shinohara, R. Kitaura, *ACS Nano* **2018**, *12*, 2498.

[53] K. L. Seyler, P. Rivera, H. Yu, N. P. Wilson, E. L. Ray, D. G. Mandrus, J. Yan, W. Yao, X. Xu, *Nature* **2019**, *567*, 66.

[54] R. Gillen, J. Maultzsch, *Phys. Rev. B* **2018**, *97*, 165306.

[55] M. Palummo, M. Bernardi, J. C. Grossman, *Nano Lett.* **2015**, *15*, 2794.

[56] S. Latini, K. T. Winther, T. Olsen, K. S. Thygesen, *Nano Lett.* **2017**, *17*, 938.

[57] E. Torun, H. P. C. Miranda, A. Molina-Sánchez, L. Wirtz, *Phys. Rev. B* **2018**, *97*, 245427.

[58] T. Deilmann, K. S. Thygesen, *Nano Lett.* **2018**, *18*, 1460.

[59] X. Lu, X. Li, L. Yang, *Phys. Rev. B* **2019**, *100*, 155416.

[60] N. Scheuschner, R. Gillen, M. Staiger, J. Maultzsch, *Phys. Rev. B* **2015**, *91*, 235409.

[61] H. P. C. Miranda, S. Reichardt, G. Froehlicher, A. Molina-Snchez, S. Berciaud, L. Wirtz, *Nano Lett.* **2017**, *17*, 2381.

[62] A. Chernikov, T. C. Berkelbach, H. Hill, A. Rigosi, Y. Li, O. B. Aslan, D. R. Reichman, M. S. Hybertsen, T. F. Heinz, *Phys. Rev. Lett.* **2014**, *113*, 076802.

[63] K. P. Dhakal, D. L. Duong, J. Lee, H. Nam, M. Kim, M. Kan, Y. H. Lee, J. Kim, *Nanoscale* **2014**, *6*, 13028.

[64] H. Li, M. Qin, L. Wang, X. Zhai, R. Ren, J. Hu, *Opt. Express* **2017**, *25*, 31612.

[65] A. Kormányos, G. Burkard, M. Gmitra, J. Fabian, V. Zólyomi, N. D. Drummond, V. Fal'ko, *2D Mater.* **2015**, *2*, 022001.

[66] D. Y. Qiu, F. H. da Jornada, S. G. Louie, *Phys. Rev. Lett.* **2015**, *115*, 119901.

[67] A. Molina-Sánchez, D. Sangalli, K. Hummer, A. Marini, L. Wirtz, *Phys. Rev. B* **2013**, *88*, 045412.

[68] G. Berghäuser, E. Malic, *Phys. Rev. B* **2014**, *89*, 125309.

[69] H. P. Komsa, A. V. Krasheninnikov, *Phys. Rev. B* **2012**, *86*, 241201.

[70] F. A. Rasmussen, K. S. Thygesen, *J. Phys. Chem. C* **2015**, *119*, 13169.

[71] R. Tempelaar, T. C. Berkelbach, *Nat. Commun.* **2019**, *10*, 3419.

[72] D. Xiao, G.-B. Liu, W. Feng, X. Xu, W. Yao, *Phys. Rev. Lett.* **2012**, *196802*.

[73] M. Staiger, R. Gillen, N. Scheuschner, O. Ochedowski, F. Kampmann, M. Schleberger, C. Thomsen, J. Maultzsch, *Phys. Rev. B* **2015**, *91*, 195419.

[74] P. C. Miranda, S. Reichardt, G. Froehlicher, A. Molina-Sánchez, S. Berciaud, L. Wirtz, *Nano Lett.* **2017**, *17*, 2381.

[75] S. Ross, P. Rivera, J. Schaibley, E. Lee-Wong, H. Yu, T. Taniguchi, K. Watanabe, J. Yan, D. Mandrus, D. Cobden, W. Yao, X. Xu, *Nano Lett.* **2017**, *17*, 638.

[76] M. M. Glazov, T. Amand, X. Marie, D. Lagarde, L. Bouet, B. Urbaszek, *Phys. Rev. B* **2014**, *89*, 201302.

[77] P. Rivera, K. L. Seyler, H. Yu, J. R. Schaibley, J. Yan, D. G. Mandrus, W. Yao, X. Xu, *Science* **2016**, *351*, 688.

[78] P. Nagler, G. Plechinger, M. V. Ballottin, A. Mitioglu, S. Meier, N. Paradiso, C. Strunk, A. Chernikov, P. Christianen, C. Schäller, T. Korn, *2D Mater.* **2017**, *4*, 025112.

[79] C. Choi, J. Huang, H.-C. Cheng, H. Kim, A. K. Vinod, S.-H. Bae, V. O. Özçelik, R. Grassi, J. Chae, S.-W. Huang, X. Duan, K. Kaasbjerg, T. Low, C. W. Wong, *2D Mater. Appl.* **2018**, *2*, 30.

[80] L. Meckbach, U. Huttner, L. C. Bannow, T. Stroucken, S. W. Koch, *J. Phys: Condens. Matter* **2018**, *30*, 374002.

[81] A. Marini, C. Hogan, M. Grüning, D. Varsano, *Comput. Phys. Commun.* **2009**, *180*, 1392.

[82] M. Rohlfing, S. G. Louie, *Phys. Rev. B* **2000**, *62*, 4927.

[83] J. J. Zhou, J. Park, I.-T. Lu, I. Maliyov, X. Tong, M. Bernardi, arXiv:2002.02045, **2020**.

[84] We used the Quantum ESPRESSO[95] package to calculate the electronic structure and phonon spectra on a uniform grid of $9 \times 9 \times 1$ k-points using the local density approximation and normconserving pseudopotentials from the PseudoDojo repository[96]. The electronic wave-functions were expanded in a planewave basis with a cutoff energy of 120 Ry, allowing for well converged phonon frequencies. We included spin-orbit coupling in our calculations and corrected the electronic structure with the GW corrections to match the electronic bands shown in Figure 6. Using the results of these results as input, we then used the PERTURBO code to calculate the temporal dynamics of excited electrons in the conduction bands. For this, we initially placed a charge of 0.1 e in the conduction band minimum at each of the K and K' points of the hexagonal Brillouin zone and propagated the band occupations through solution of the Boltzmann

Transport Equation including electron-phonon coupling induced scattering for a simulation time of 2 ps and temperatures of 10 and 300 K. To ensure an accurate representation of the scattering processes, a wannierization procedure was used to interpolate the electron-phonon matrix elements from a coarse $9 \times 9 \times 1$ k-point grid to a dense $90 \times 90 \times 1$ grid.

[85] T. Woźniak, P. E. Faria Junior, G. Seifert, A. Chaves, J. Kunstmann, *Phys. Rev. B* **2020**, *101*, 235408.

[86] T. Deilmann, P. Krüger, M. Rohlfing, *Phys. Rev. Lett.* **2020**, *124*, 226402.

[87] J. Förste, N. V. Tepliakov, S. Y. Kruchinin, J. Lindlau, V. Funk, M. Förg, K. Watanabe, T. Taniguchi, A. S. Baimuratov, A. Högele, *Nat. Commun.* **2020**, *11*, 4539.

[88] M. Roth, *Phys. Rev.* **1960**, *118*, 1534.

[89] The values for the indirect excitons were obtained from calculations with a rather coarse $12 \times 12 \times 1$ k-point grid, but explicit inclusion of spin-orbit coupling in the BSE calculations.

[90] T. P. Lyons, S. Dufferwiel, M. Brooks, F. Withers, T. Taniguchi, K. Watanabe, K. S. Novoselov, G. Burkard, A. I. Tartakovskii, *Nat. Commun.* **2019**, *10*, 2330.

[91] C. Berkelbach, M. S. Hybertsen, D. R. Reichman, *Phys. Rev. B* **2013**, *88*, 045318.

[92] H. Yu, G.-B. Liu, P. Gong, X. Xu, W. Yao, *Nat. Commun.* **2014**, *5*, 3876.

[93] A. Mostofi, J. R. Yates, G. Pizzi, Y.-S. Lee, I. Souza, D. Vanderbilt, N. Marzari, *Comput. Phys. Commun.* **2014**, *185*, 2309.

[94] R. Hamann, *Phys. Rev. B* **2013**, *88*, 085117.

[95] P. Giannozzi, S. Baroni, N. Bonini, M. Calandra, R. Car, C. Cavazzoni, D. Ceresoli, G. L. Chiarotti, M. Cococcioni, I. Dabo, A. D. Corso, S. de Gironcoli, S. Fabris, G. Fratesi, R. Gebauer, U. Gerstmann, C. Gougoussis, A. Kokalj, M. Lazzeri, L. Martin-Samos, N. Marzari, F. Mauri, R. Mazzarello, S. Paolini, A. Pasquarello, L. Paulatto, C. Sbraccia, S. Scandolo, G. Sclauzero, A. P. Seitsonen, A. Smogunov, P. Umari, R. M. Wentzcovitch, *J. Phys.: Condens. Matter* **2009**, *21*, 395502.

[96] M. J. van Setten, M. Giantomassi, E. Bousquet, M. Verstraete, D. Hamann, X. Gonze, G.-M. Rignanese, *Comput. Phys. Commun.* **2018**, *226*, 39.

[97] H. da Jornada, D. Y. Qiu, S. G. Louie, *Phys. Rev. B* **2017**, *95*, 035109.

[98] The G_0W_0 simulations in Figure 1 were performed with the BerkeleyGW code, using 2000 unoccupied bands in combination with the static remainder method to account for higher-energy interband transitions. The band energies were extrapolated to infinite cutoff energy for the correlation contribution with the method we employed previously in Ref. [54] and calculations for cutoff energies of 250, 300 and 350 eV, for which the variation of band energies is linear with the inverse of the number of included reciprocal lattice vectors. A homogeneous 9×9 k-point grid together with the "Nonuniform Neck Subsampling" method[97] was sufficient to converge the electronic bandgap to less than 0.05 eV. The effect of spin-orbit interaction was included a posteriori by extracting the spin-orbit-induced band splittings on the DFT level of theory and adding the extracted values to the GW band energies. The electronic band structures were calculated through Wannier interpolation using the Wannier 90[93] code. The input electronic energies and wavefunctions and the groundstate density for the GW and Wannier calculations were computed with the Quantum ESPRESSO code, optimized norm-conserving Vanderbilt pseudopotentials,[94] a cutoff energy of 90 Ry and a $12 \times 12 \times 1$ k-point grid (for the groundstate calculations). The atomic positions and lattice vectors were relaxed using the method outlined in Ref. [21].

[99] A. Molina-Sánchez, M. Palummo, A. Marini, L. Wirtz, *Phys. Rev. B* **2016**, *93*, 155435.